AGU ADVANCING EARTH AND SPACE SCIENCES

Earth and Space Science

RESEARCH ARTICLE
10.1029/2023EA003499

Bias-Eliminating Techniques in the Computation of Power Spectra for Characterizing Gravity Waves: Interleaved Methods and Error Analyses

Jackson Jandreau[1,2] **and Xinzhao Chu**[1,2]

[1]Cooperative Institute for Research in Environmental Sciences, University of Colorado Boulder, Boulder, CO, USA, [2]Department of Aerospace Engineering Sciences, University of Colorado Boulder, Boulder, CO, USA

Key Points:

- We develop an interleaved data processing technique to compute cross-power spectral density (CPSD) for deriving unbiased wave spectra
- Accuracy and precision analyses of coincident-power spectral density (Co-PSD) and CPSD magnitude show Co-PSD eliminating noise floor entirely
- The spectral interleaved method is shown to eliminate noise floor, demonstrated using a forward model and Antarctic lidar observations

Correspondence to:

X. Chu and J. Jandreau,
Xinzhao.Chu@colorado.edu;
Jackson.Jandreau@colorado.edu

Citation:

Jandreau, J., & Chu, X. (2024). Bias-eliminating techniques in the computation of power spectra for characterizing gravity waves: Interleaved methods and error analyses. *Earth and Space Science*, *11*, e2023EA003499. https://doi.org/10.1029/2023EA003499

Received 29 DEC 2023
Accepted 8 SEP 2024

Author Contributions:

Conceptualization: Jackson Jandreau, Xinzhao Chu
Data curation: Jackson Jandreau, Xinzhao Chu
Formal analysis: Jackson Jandreau, Xinzhao Chu
Funding acquisition: Xinzhao Chu
Investigation: Jackson Jandreau, Xinzhao Chu
Methodology: Jackson Jandreau, Xinzhao Chu
Project administration: Xinzhao Chu
Resources: Xinzhao Chu
Software: Jackson Jandreau
Supervision: Xinzhao Chu
Validation: Jackson Jandreau, Xinzhao Chu
Visualization: Jackson Jandreau

Abstract Observational data inherently contain noise which manifests as uncertainties in the measured parameters and creates positive biases or noise floors in second-order products like variances, fluxes, and spectra. Historical methods estimate and subsequently subtract noise floors, but struggle with accuracy. Gardner and Chu (2020, doi.org/10.1364/AO.400375) proposed an interleaved data processing method, which inherently eliminates biases from variances and fluxes, and suggested that the method could also eliminate noise floors of power spectra. We investigate the interleaved method for spectral analysis of atmospheric waves through theoretical studies, forward modeling, and demonstration with lidar data. Our work shows that calculating the cross-power spectral density (CPSD) from two interleaved subsamples does reduce the spectral noise floor significantly. However, only the Co-PSD (the real part of CPSD) eliminates the noise floor completely, while taking the absolute magnitude of CPSD adds a reduced noise floor back to the spectrum when the sample number is finite. This reduced noise floor can be further minimized through averaging over more observations, completely different from traditional spectrum calculations whose noise floor cannot be reduced by incorporating more samples. We demonstrate the first application of the interleaved method to spectral data, successfully eliminating the noise floor using the Co-PSD in a forward model and in lidar observations of the vertical wavenumber of gravity waves at McMurdo, Antarctica. This high accuracy is gained by sacrificing precision due to photon-count splitting, requiring additional observations to counter this effect. We provide quantitative assessment of accuracy and precision as well as application recommendations.

Plain Language Summary Atmospheric waves serve a vital role in global energy and momentum transportation between the lower and upper atmosphere, driving major atmospheric circulations. These waves exist across many scales, from large planetary waves to medium- and small-scale gravity waves (GW). GW are a key factor driving many atmospheric phenomena, but due to their relatively smaller scales, they are difficult to study. The spectra of GW are important to understanding wave dynamics and informing the development of atmospheric models, as these spectra contain critical information about how wave-transported energy is distributed amongst different temporal and spatial frequencies. A major tool in improving our knowledge and modeling of GW is their direct observations. Although being powerful wave observation tools, lidar and radar data contain noise in their measurements which manifests as noise floors, obscuring derived wave power spectra. These floors cannot be removed by averaging more samples, as is done for other parameters, making it difficult to accurately interpret the spectra. Pre-existing techniques can remove this floor, but they struggle with accuracy, especially in high-noise conditions. This study introduces and demonstrates the use of an interleaved method of spectral processing, which eliminates the noise floors altogether, enabling high-accuracy calculation of wave spectra.

1. Introduction

The computation of power spectra is an important task to characterize wave dynamics using lidar, radar, and other remote sensing data over the whole atmosphere as well as geospace. However, as pointed out by Gardner and Chu (2020), conventional spectral analysis techniques result in noise floors established by the white noise (e.g., the lidar photon noise or radar noise power) in the detection processes. Such noise floors could obscure waves with weak amplitudes, significantly limiting the detectable spectral ranges of atmospheric waves. Similarly, the computations of other second-order parameters, such as variances and fluxes, also suffer positive biases induced by noise. Without proper subtraction or elimination, these noise floors and biases can conceal real geophysical

Writing – original draft: Jackson Jandreau, Xinzhao Chu
Writing – review & editing: Jackson Jandreau, Xinzhao Chu

features or cause misleading results (Chu et al., 2018; Gardner & Chu, 2020; Gardner & Liu, 2014; Jandreau & Chu, 2022; Lu et al., 2015).

A novel idea, that is, the interleaved data processing technique, was proposed by Gardner and Chu (2020) to eliminate biases and noise floors in the second-order statistics of wave perturbations in observational data. This interleaved technique separates raw data into two subsamples of the odd and even bins, respectively, then derives two sets of independent measurements that are basically simultaneous and common-volume, and finally computes covariances, cross-fluxes, or cross-power spectra between the two measurements, which retain the geophysical features of variances, fluxes, or power spectra but possess zero biases due to the zero-mean and uncorrelated noise from the two independent measurements. In that historic paper, Gardner and Chu (2020) performed the theoretical analyses of the interleaved principles, demonstrated the bias-eliminating techniques in the computation of temperature and lapse rate variances, and provided the equations of interleaved techniques for the computations of variances, fluxes, and power spectra. Later, the computations of vertical fluxes of sensible heat and meteoric Na, variances of temperature, vertical wind and Na density, and potential energy of gravity waves using the interleaved techniques, were demonstrated on the lidar measurements over McMurdo, Antarctica, which led to the discovery of upward sensible heat fluxes in the lower thermosphere (Chu et al., 2022).

It is worth noting that the interleaved approach to noise-bias elimination is very different from the conventional correction techniques that compute the second-order statistics containing the biases or noise floors, then estimate the biases or noise floors, and finally subtract them from the initial computations. In contrast, the interleaved techniques eliminate the biases or noise floors from the beginning of calculation, and then average over many samples to reduce the uncertainties. The resultant variances, fluxes, and power spectra are basically free of biases and noise floors, that is, very high accuracy, but still contain uncertainties (i.e., imprecisions) induced by noise. Accuracy and precision are two different concepts in error analysis, but they easily cause confusion. Exact definitions of these two concepts will be provided in Section 2. Jandreau and Chu (2022) analyzed existing methods in calculating variances and gravity-wave potential energy to handle noise-induced biases in the spatial-temporal domain (Chu et al., 2018; Gardner & Chu, 2020; Whiteway & Carswell, 1995), specifically comparing the two conventional bias-subtraction methods against the interleaved bias-elimination method, and finding that the interleaved method was especially powerful and enabled the use of data which was not useable via the other existing methods. Certainly, one has the freedom in choosing the technique implementation fashion from the time-interleaved method (Chu et al., 2022; Gardner & Chu, 2020) to the altitude-interleaved method (Jandreau & Chu, 2022). It is necessary to mention that the interleaved method shares a similar principle as the time-lagged method proposed in Gardner and Liu (2014), that is, separating data into two independent subsamples so that noise from the two subsample measurements is uncorrelated thus eliminated via averaging over many samples. Of course, the interleaved idea is more elegant than the time-lagged method on the aspect of minimizing the time or altitude shift between the two subsample measurements thus achieving the highest possible accuracy (see details in Section 2).

To date, the computation of power spectra using the interleaved technique has not been demonstrated in literature. Gardner and Chu (2020) have provided an equation for estimating temporal frequency spectrum—their Equation 28, which involves taking the discrete Fourier transforms (DFT) for deriving spectral amplitudes from the odd- and even-bin measurements, respectively, and then calculating the cross-spectrum from these two independent DFT amplitudes, averaging the cross-spectrum over many samples, and finally computing the absolute magnitude of the mean cross-spectrum. However, our studies have shown that Equation 28 in Gardner and Chu (2020) may not be optimal for computing wave power spectra because the absolute magnitude does not entirely remove bias under high noise conditions but adds a reduced noise floor back to the spectra (see Section 2.2). In contrast, taking only the real part of the cross-spectrum, that is, the coincident-spectrum (co-spectrum) as practiced in meteorology studies (Stull, 1999), does eliminate the noise floor entirely; however, this co-spectrum is slightly smaller than the true wave power spectrum. Therefore, it is imperative to analyze these two methods—taking the co-spectrum or the absolute magnitude of cross-spectrum—in detail and properly assess the accuracy and precision of the interleaved power spectra.

To address the above issues, this study focuses on the development of spectral interleaved techniques for eliminating the noise floors from the computed power spectra while maintaining energy conservation in the derivation of cross-power spectra, and on the related error analyses of spectral accuracy and precision, especially the derivations of spectral uncertainties. This paper compares the interleaved method with the existing methods

for noise-bias correction in power spectrum calculations, determines the conditions in which each method should be used, and investigates how these methods correspond to similar methods applied in the space-time domain to correct variances via covariances. This study is done by examining the theories behind the methods, by forward modeling, and by applications to real data collected during the 10-year McMurdo lidar observations with an aim of calculating vertical-wavenumber spectra of gravity waves observed over McMurdo, Antarctica. While these techniques are demonstrated using lidar data and discussed in terms of photon counts and lidar terms, it should be possible to apply the techniques to a wide variety of observational data sets including radar and other remote sensing and in-situ observations of the atmosphere and space. The ideas and principles of interleaved techniques and spectral uncertainty derivations are applicable to various observations within and outside the atmosphere and space sciences.

2. Interleaved Data Processing Techniques for Deriving Spectra of Waves

Lidar measurements of atmospheric densities are employed in this study to illustrate the various methods in deriving wave spectra and variances. Statistics performed here have assumed that the atmospheric density observations as well as measurements of other atmospheric parameters, such as temperatures, winds, species densities, and backscatter coefficients, etc., are samples of stationary, ergodic random processes (Bendat & Piersol, 2010; Gardner & Chu, 2020). Therefore, the sample average can be used to approximate the ensemble average (Bendat & Piersol, 2010; Gardner & Chu, 2020; Jandreau & Chu, 2022) in the limit of a very large number of samples.

In studying atmospheric wave data of any kind, pushing to higher resolutions of data will always be limited by some noise limit which is inherent to the photon counting process and cannot be avoided. The shot noise manifests as a zero-mean perturbation uncertainty ($\Delta\rho$) alongside the zero-mean tracer perturbation (ρ'), in this case atmospheric density, as in Equation 1a and due to the linearity of the discrete Fourier transform (DFT), can be represented as Equation 1b.

$$\rho'_{Total}(z,t) = \rho'(z,t) + \Delta\rho(z,t) \tag{1a}$$

$$DFT\left(\rho'_{Total}\right) = DFT\left(\rho' + \Delta\rho\right) = DFT\left(\rho'\right) + DFT(\Delta\rho) \tag{1b}$$

where ρ'_{Total} represents the total perturbation consisting of both wave and noise induced perturbations, and where z and t are altitude and time, respectively. To simplify expressions, the DFT here refers to a 1-D Fourier transform, which could be with respect to z or t.

Uncertainties induced by this noise can be minimized through sample averaging for first-order parameters like atmospheric temperatures, densities, and perturbations, where the incorporation of additional samples drives the noise term toward zero. However, in calculating second-order atmospheric parameters (Equations 2) like variances, fluxes, and spatial and temporal energy/power spectra, the parameters are positively biased by these noise effects and additional data averaging does not reduce the bias. This bias is the final term of Equations 2a and 2b, a positive offset in the variance term, and a noise floor in the spectral one:

$$Var\left(\rho'_{Total}\right) = \left\langle [\rho'(z,t) + \Delta\rho(z,t)]^2 \right\rangle = \left\langle [\rho']^2 \right\rangle + \left\langle 2\rho'\Delta\rho \right\rangle + \langle [\Delta\rho]^2 \rangle = \left\langle [\rho']^2 \right\rangle + \langle [\Delta\rho]^2 \rangle \tag{2a}$$

$$\begin{aligned} Power\ Spectra &= \left\langle DFT\left(\rho'_{Total}\right) DFT\left(\rho'_{Total}\right)^* \right\rangle \\ &= \left\langle |DFT(\rho')|^2 \right\rangle + \left\langle 2DFT\left(\rho'\right) DFT^*(\Delta\rho) \right\rangle + \langle |DFT(\Delta\rho)|^2 \rangle = \left\langle |DFT(\rho')|^2 \right\rangle + \langle |DFT(\Delta\rho)|^2 \rangle \end{aligned} \tag{2b}$$

where *Var* is the variance operator, DFT denotes a standard discrete Fourier transform operation, the asterisk indicates a complex conjugate, and the angle brackets denote an ensemble average, that is, the expectation of the variable. The last equal signs are achieved in Equations 2a and 2b because we realize that the expectations of the cross terms in Equations 2a and 2b are zero when ρ' and $\Delta\rho$ as well as $DFT(\rho')$ and $DFT^*(\Delta\rho)$ are uncorrelated. This conclusion depends on the relations,

$$\langle \Delta\rho(z,t)\rangle = \lim_{N\to\infty}\frac{1}{N}\sum_{k=1}^{N}\Delta\rho(z_k,t) = 0 \tag{3a}$$

$$\langle DFT(\Delta\rho(z,t))\rangle = \lim_{N\to\infty}\frac{1}{N}\sum_{k=1}^{N}DFT(\Delta\rho(z_k,t)) = DFT\left[\lim_{N\to\infty}\frac{1}{N}\sum_{k=1}^{N}\Delta\rho(z_k,t)\right] = DFT(0) = 0 \tag{3b}$$

and the cross-terms in Equations 2a and 2b are driven toward zero as more observations are included. The relation in Equation 3 is true for an average over z or t. This relation is also critical to the performance of the interleaved method, as will be demonstrated in Section 2.2. Even in the case of minor photon noise, the presence of $\langle[\Delta\rho]^2\rangle$ or $\langle|DFT(\Delta\rho)|^2\rangle$ guarantees a non-zero noise floor, biasing the variances and spectra positively by some amount. In cases where the strength of the noise perturbations approach that of the waves interested, the entire signal may be unusable without correction.

Two techniques which can be used to estimate and subtract the noise bias in the variance domain are referred to as the variance subtraction technique and the spectral proportion technique with the latter one proposed and demonstrated in Chu et al. (2018). They are two different approaches used to estimate the $\langle[\Delta\rho]^2\rangle$, with the former relying on analytical equations under certain assumptions of noise distributions and the latter using a graphical determination of noise floors to estimate the $\langle[\Delta\rho]^2\rangle$. Both techniques are summarized and compared in Jandreau and Chu (2022). Correspondingly, there are two similar techniques in the spectral domain for estimating the $\langle|DFT(\Delta\rho)|^2\rangle$ and then subtract the estimated noise floors from the PSD (see a summary in Section 2.1). Certainly, it is challenging to derive an accurate estimate of $\langle[\Delta\rho]^2\rangle$ or $\langle|DFT(\Delta\rho)|^2\rangle$. The interleaved method addresses this challenge by systematically eliminating the noise biases or noise floors without the need of estimating the noise biases/floors (see Section 2.2 for details).

For dealing with the noise floor in spectral analysis, one of two approaches must be taken: Limiting studies to the range of spectra whose strengths are above the noise floor or removing the noise floor somehow. There have been a few conventional approaches to removing the noise floor as mentioned above, each is elaborated upon in Section 2.1. Noise floor correction allows the extension of spectral studies into the higher resolution portion of the spectrum that was previously obscured by the noise floor yet can be especially critical for results incorporating higher frequency or larger wave-number waves, turbulent regimes, or in utilizing data taken under noisy conditions.

2.1. Previously Available Techniques for Noise Subtraction

Ultimately, the results shown in Section 3 will be those of vertical wavenumber (m) power spectral density (PSD), scaled from a DFT via the periodogram method as in Dewan and Grossbard (2000) and Heinzel et al. (2002), and all spectral terms hereafter will be in terms of this PSD scaling. This is calculated for spatial and temporal spectra as follows

$$PSD_\rho(m) = \frac{2\Delta z}{N_{unpad}}\overline{|DFT(\rho(z,t))|^2} \tag{4a}$$

$$PSD_\rho(\omega) = \frac{2\Delta t}{N_{unpad}}\overline{|DFT(\rho(z,t))|^2} \tag{4b}$$

where Δz and Δt are the spatial and temporal resolutions of $\rho(z,t)$. The single-sided DFT is used in Equations 4a and 4b, thus the factor of two in their numerators. It is worth noting that if zero-padding is used in calculating the DFT, then the unpadded N length, N_{unpad}, should be used in the PSD scaling to reveal the true wave power that is given by the integrated area below the PSD envelope. The PSDs in Equations 4a and 4b are shown with an overbar to denote the sample averaging of multiple spatial/temporal spectra, respectively, together. This is done to emphasize that with real data, such averaging is necessary to reduce uncertainty, as well as to keep notation similar to Equations 7a and 7b where such averaging is also used in the interleaved method.

The first approach to removing the noise floor from the PSD is to calculate the value of the noise floor in the data based on the photon noise model which traces noise from photon counts directly into its spectral strength. This method will be referred to as the calculative subtraction method. Gardner et al. (1989) gives an example of such a PSD correcting equation which yields an estimate of the noise floor based on photon counts, accounting for certain filtering characteristics. This equation can also be written simply in terms of the relative parameter uncertainty where Equation 5a shows the noise floor for one-sided vertical wavenumber spectrum at a given time, and Equation 5b shows the noise floor for a one-sided temporal spectrum at a given altitude:

$$PSD_{Floor,m} = \frac{2\Delta z}{N_z N_t} \sum_{n=1}^{N_t} \sum_{k=1}^{N_z} \left(\frac{\delta\rho(z_k, t_n)}{\rho(z_k, t_n)} \right)^2 \tag{5a}$$

$$PSD_{Floor,\omega} = \frac{2\Delta t}{N_t N_z} \sum_{n=1}^{N_t} \sum_{k=1}^{N_z} \left(\frac{\delta\rho(z_k, t_n)}{\rho(z_k, t_n)} \right)^2 \tag{5b}$$

where the calculation of the δ parameter error term may differ from application to application. The δ error in this study was calculated as in Chu et al. (2018). Because the photon noise in each resolution cell (i.e., range bin or time bin) is statistically independent of the photon noise in every other cell, the noise spectrum is white, that is, constant noise floor at all frequencies and wave numbers, consistent with the expected PSD of the assumed noise model. This calculative noise-floor-subtraction approach is based on the same principle as the variance subtraction method mentioned in Section 1 and shares the same drawbacks for spectral analysis as it does in variance/flux applications. Chu et al. (2018), Gardner and Chu (2020), and Jandreau and Chu (2022) each detail that the major drawback of this approach is that when the strength of the noise variance approaches that of the wave variance, often the resulting variance is negative. When discussing wave energies, the wave energy cannot physically be negative which obviously invalidates this approach for those cases. This issue occurs mainly because the measurement error terms are estimated from the measured photon counts by linearizing the nonlinear system equations (Gardner & Chu, 2020). When noise is high, the omitted higher-order terms (like the second and third orders) may become comparable to the first-order linear terms. Coupled with the need for an accurate noise model, accurate estimates of errors are basically impossible when noise levels are high. This same "negative energy" result is obtained when applying this method to spectral correction of real data taken under high-noise conditions.

The second approach to correct the noise floor of a spectrum is to estimate the noise floor by inspection based on the shape of the derived spectrum, referred to hereafter in this study as the (noise floor) graphical subtraction method. This method has been used with success by Wilson et al. (1991) and is comparable to the spectral proportion technique used by Chu et al. (2018) for correcting noise-induced variance. Here, a noise floor is estimated based on the high-resolution portion of the data's PSD, essentially visually or algorithmically using the shape of the spectra to identify the noise floor, and this estimate is subtracted from the PSD to remove the noise floor. Because higher-order nonlinear terms are naturally included in the formation of the floor, this graphical subtraction method usually works better than the analytical one above when noise is high. In this study, the three lowest minima were selected from the last 25% of the uncorrected PSD and their values were averaged to estimate the noise floor. It was observed that results improved when more samples are averaged together before applying this floor-selection algorithm, as this allowed for the floor to "be flattened" before selection. This noise-floor selection criterion was selected for use in the spectral proportion after much testing was done by Jandreau and Chu (2022) and is similar to the noise-floor-selection criteria used by Chu et al. (2018). While this approach could work relatively well in many cases, there may exist certain spectra which this method struggles with, such as if the true (not-noise) spectrum was especially flat, the approach could easily misidentify the noise floor. Generally, spectral shape will not cause issues if the user is cautious about floor-selection criteria; however, there will always be difficult-to-quantify uncertainties in such a "manual" method of noise floor estimation. What is more commonly seen is that application to a spectrum whose floor is not fully developed often results in mis-estimation of the floor magnitude and thus an incorrect subtraction, leaving remnants of floor in the spectra and thus overestimating the PSD values at higher frequencies.

2.2. Interleaved Techniques

The previous two methods aim to subtract the noise floor from the total spectra that consist of both wave spectra and noise spectra. In contrast, for the most recently developed approach by Gardner and Chu (2020), the interleaved data processing technique eliminates the noise bias outright, instead of computing a quantity for the bias and subtracting it, as was done in the two prior methods. This interleaved method takes advantage of the fact that the noise-induced perturbations in the measured photons are uncorrelated between two independent samples and are also statistically independent from the wave induced perturbations in the signal. The interleaved method is implemented by breaking the photon counts into two subsamples of the odd and even bins, ρ_A and ρ_B, and replacing the variance parameter with a covariance, or in the spectral domain, replacing the PSD with cross-power spectral density (CPSD) magnitude or the CPSD real part—coincident-power spectral density (Co-PSD). The definitions of CPSD and Co-PSD and their relations are given below in terms of the sample average represented by the overbar.

$$CPSD\left(\rho'_{A,Total}, \rho'_{B,Total}\right) = \frac{2\Delta z}{N_z}\overline{DFT\left(\rho'_{A,Total}\right)DFT^*\left(\rho'_{B,Total}\right)} \tag{6a}$$

$$Co\text{-}PSD\left(\rho'_{A,Total}, \rho'_{B,Total}\right) = Re\left[CPSD\left(\rho'_{A,Total}, \rho'_{B,Total}\right)\right] \tag{6b}$$

$$Q\text{-}PSD\left(\rho'_{A,Total}, \rho'_{B,Total}\right) = Im\left[CPSD\left(\rho'_{A,Total}, \rho'_{B,Total}\right)\right] \tag{6c}$$

where the real and imaginary parts of CPSD are termed the Coincident-PSD (Co-PSD) and the Quadrature-PSD (Q-PSD), respectively (Bendat & Piersol, 2010; von Storch & Zwiers, 1999; Stull, 1999). There are two options in the interleaved spectral analysis. One is to take the absolute magnitude of the mean CPSD as suggested in Gardner and Chu (2020), and another is to take the Co-PSD, that is, the real part of CPSD, without calculating absolute magnitudes as explored in this study. In Equation 7, which formulates the interleaved data processing techniques for variance and spectral analysis, we present the options of Co-PSD and CPSD magnitude in Equations 7b and 7c, respectively.

$$\begin{aligned} &Cov\left[\rho'_{A,Total}(z_A), \rho'_{B,Total}(z_B)\right] \\ &= \overline{\left[\rho'_A(z_A, t)\cdot \rho'_B(z_B, t)\right]} + \overline{\left[\rho'_A(z_A, t)\cdot \Delta\rho_B(z_B, t)\right]} \\ &+ \overline{\left[\rho'_B(z_B, t)\cdot \Delta\rho_A(z_A, t)\right]} + \overline{\left[\Delta\rho_A(z_A, t)\cdot \Delta\rho_B(z_B, t)\right]} \\ &\simeq \overline{\left[\rho'_A(z_A, t)\cdot \rho'_B(z_B, t)\right]} = Cov\left[\rho'_A(z_A, t), \rho'_B(z_B, t)\right] \end{aligned} \tag{7a}$$

$$\begin{aligned} Co\text{-}PSD\left(\rho'_{A,Total}, \rho'_{B,Total}\right) &= \frac{2\Delta z}{N_z} Re\left[\overline{DFT\left(\rho'_{A,Total}\right)DFT^*\left(\rho'_{B,Total}\right)}\right] \\ &= \frac{2\Delta z}{N_z} Re\left[\overline{\left(DFT\left(\rho'_A\right) + DFT(\Delta\rho_A)\right)\left(DFT\left(\rho'_B\right) + DFT(\Delta\rho_B)\right)^*}\right] \\ &= \frac{2\Delta z}{N_z} Re\left[\begin{array}{c}\overline{DFT\left(\rho'_A\right)DFT^*\left(\rho'_B\right) + DFT\left(\rho'_A\right)DFT^*(\Delta\rho_B)} \\ +DFT(\Delta\rho_A)DFT^*\left(\rho'_B\right) + DFT(\Delta\rho_A)DFT^*(\Delta\rho_B)\end{array}\right] \\ &\simeq \frac{2\Delta z}{N_z} Re\left[\overline{DFT\left(\rho'_A\right)DFT^*\left(\rho'_B\right)}\right] = Co\text{-}PSD\left(\rho'_A, \rho'_B\right) \end{aligned} \tag{7b}$$

$$\left|CPSD\left(\rho'_{A,Total}, \rho'_{B,Total}\right)\right| = \frac{2\Delta z}{N_z}\left|\overline{DFT\left(\rho'_{A,Total}\right)DFT^*\left(\rho'_{B,Total}\right)}\right| \tag{7c}$$

where $\rho'_{A,Total} = \rho'_A + \Delta\rho_A$ and $\rho'_{B,Total} = \rho'_B + \Delta\rho_B$ are the total perturbations in the two subsamples of odd- and even-bin measurements, respectively. Here ρ'_A and ρ'_B represent the purely wave-induced tracer perturbations, and $\Delta\rho_A$ and $\Delta\rho_B$ are the noise-induced perturbation uncertainties at the corresponding altitudes z_A and z_B of the odd- and even-bin measurements, respectively. Equations 7b and 7c are written for the calculation of vertical wavenumber spectra, where the Fourier transforms taken are of vertical profiles and the DFT here is one-sided (thus the factor of two in the numerator), the N_z is the unpadded length of said vertical profiles, and the resolution Δz is the step size of the spatial series. For calculating a temporal spectrum, the dimensions of the overbar average would be switched and N_t and Δt used instead.

The interleaved techniques shown in Equations 7a and 7b reveal the true wave-induced covariance and Co-PSD by utilizing the aforementioned statistical independence between two interleaved subsamples (A and B) and between the wave-induced and noise-induced perturbations. The expectations of the cross terms in Equation 7 are zero:

$$\left\langle \rho'_A(z_A, t)\cdot\Delta\rho_B(z_B, t)\right\rangle = \left\langle \rho'_B(z_B, t)\cdot\Delta\rho_A(z_A, t)\right\rangle = \left\langle \Delta\rho_A(z_A, t)\cdot\Delta\rho_B(z_B, t)\right\rangle = 0 \tag{8a}$$

$$\left\langle DFT\left(\rho'_A\right) DFT^*\left(\Delta\rho_B\right)\right\rangle = \left\langle DFT\left(\Delta\rho_A\right) DFT^*\left(\rho'_B\right)\right\rangle = \left\langle DFT\left(\Delta\rho_A\right) DFT^*\left(\Delta\rho_B\right)\right\rangle = 0 \tag{8b}$$

The overbars in Equation 7 represent the sample averages, not the ensemble averages required by expectation operations to drive the cross terms to zero, which explain the approximately equal sign ($\simeq$) used in Equations 7a and 7b. Although these cross terms are not necessarily zero under limited sample averages, they represent uncertainties to the covariance and Co-PSD, but they are certainly not the systematic biases as in Equation 2. In Section 2.3 we will quantitatively consider the number of samples which must be averaged together to achieve a desired uncertainty.

Gardner and Chu (2020) provide a quantitative analysis on the correction factor between this interleaved method's covariance and the actual variance of the wavefield, and find that under typical lidar resolutions, the covariance is only a fraction of a percent smaller than the variance, and thus the covariance can essentially represent the variance. In the spectral domain, the Co-PSD can often represent the true wave-induced PSD because the sum over all wavenumbers or frequencies of Co-PSD corresponds to the covariance in the time and spatial domains (Stull, 1999). The correction factor for the Co-PSD depends on the shift δz or δt between two subsamples as well as on the wavenumbers or frequencies of waves considered. It is critical that the splitting of the raw data into the two subsamples must be done in an "interleaved" manner (Figure 1), keeping the temporal or spatial shift (δz or δt) between the subsamples to a minimum, in order to maximize the wave coherency between the two samples and minimize the correction factors. It is this interleaving scheme that sets this approach apart from previous approaches with similar principles like the "time-lagged" method proposed by Gardner and Liu (2014) and illustrated in Jandreau and Chu (2022). The correction factor will be discussed quantitatively in Section 2.3.

Figure 1 illustrates the implementation of interleaving schemes in both time and altitude domains. The interleaving can be done in either time or altitude domain and must be done such that all the even-numbered bins are in one sample and the odd-numbered ones are in the other sample. The time and spatial spectra can be calculated similarly regardless of the interleaving scheme, as Figure 1 also shows.

Using Co-PSD in Equation 7b, instead of the absolute magnitude of sample averaged CPSD as given in Equation 7c, for the interleaved spectral computation, is a further development from the originally proposed Equation 28 in Gardner and Chu (2020), which is the basis of Equation 7c. Our tests have shown that the approach in Equation 7c, that is, averaging the instantaneous or point CPSD over many samples and then taking the magnitude of that mean CPSD, does significantly reduce the noise floor compared to the uncorrected PSD given by Equation 4; however, taking the magnitude (i.e., the absolute value) adds a new, reduced noise floor back to the power spectral density. To provide a theoretical explanation, we define the instantaneous or point $CPSD_{inst}$ and its relationship with the sample-averaged $CPSD$ in Equation 9:

$$CPSD_{inst} \equiv \frac{2\Delta z}{N_z}\left(DFT_A \cdot DFT_B^*\right) = Co_{inst} + \Delta Co_{inst} + i(Q_{inst} + \Delta Q_{inst}) \tag{9a}$$

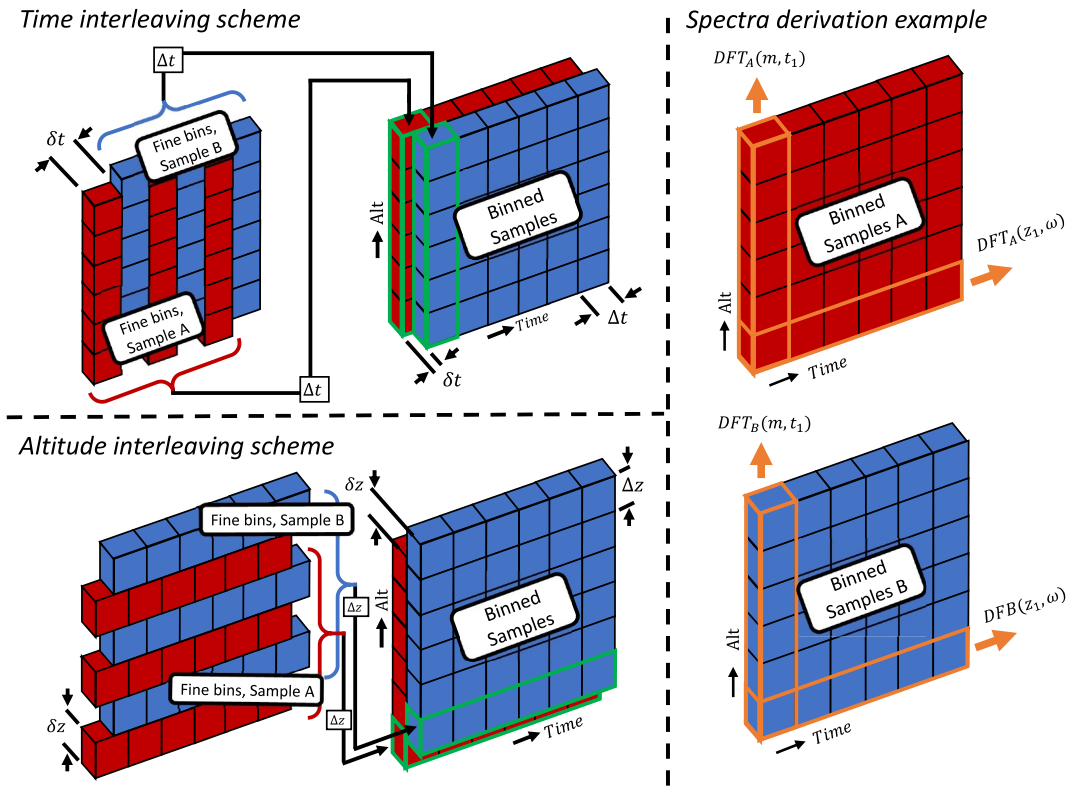

Figure 1. Diagram of the interleaved method being applied in both time interleaving and altitude interleaving, as well as a demonstration of how all spectra can be derived from either method. Typical δt and δz are small, for example, 4.5 s and 24 m in Chu et al. (2022) and Gardner and Chu (2020) or 1 min and 48 m in Jandreau and Chu (2022) and this study. Typical Δt and Δz are much larger, for example, 2.5 min and 960 m in Chu et al. (2022) or 1 hr and 480 m in this study.

$$CPSD = \overline{CPSD_{inst}} = \frac{1}{L}\sum_{n=1}^{L}[Co_{inst,n} + \Delta Co_{inst,n} + i(Q_{inst,n} + \Delta Q_{inst,n})] \quad (9b)$$

$$= Co + \Delta Co + i(Q + \Delta Q)$$

$$Co = \overline{Co_{inst}},\ Q = \overline{Q_{inst}},\ \Delta Co = \overline{\Delta Co_{inst}},\ \Delta Q = \overline{\Delta Q_{inst}} \quad (9c)$$

where $i^2 = -1$, Co and Q represent the purely wave-induced Co-PSD and Q-PSD, respectively, and ΔCo and ΔQ represent the noise-induced Co-PSD and Q-PSD. The subscription "inst" denotes instantaneous or point values, and the overbars represent taking the average over L number of samples. The absolute magnitude of CPSD and the Co-PSD are expressed as:

$$|CPSD| = \sqrt{(Co + \Delta Co)^2 + (Q + \Delta Q)^2} = \sqrt{Co^2 + Q^2 + 2Co\Delta Co + 2Q\Delta Q + (\Delta Co)^2 + (\Delta Q)^2} \quad (10a)$$

$$Co\text{-}PSD = Re(CPSD) = Co + \Delta Co \quad (10b)$$

With a finite number (L) of samples, $\Delta Co \neq 0$ and $\Delta Q \neq 0$; therefore, the terms of $(\Delta Co)^2 + (\Delta Q)^2$ in Equation 10a induce a new but reduced noise floor to the CPSD magnitude (reduced significantly from the original noise floor caused by $(\Delta Co_{inst})^2 + (\Delta Q_{inst})^2$), while the two cross terms $(2Co\Delta Co + 2Q\Delta Q)$ in Equation 10a induce reduced uncertainties to the CPSD magnitude but not biases. Equation 10a proves that the CPSD magnitude contains a non-zero noise floor at a finite number of samples.

By contrast, when considering only the CPSD real part, that is, the Co-PSD given by Equation 10b, the only noise term left (ΔCo) represents a reduced uncertainty but not a bias. Because the noise term is not squared and it can be

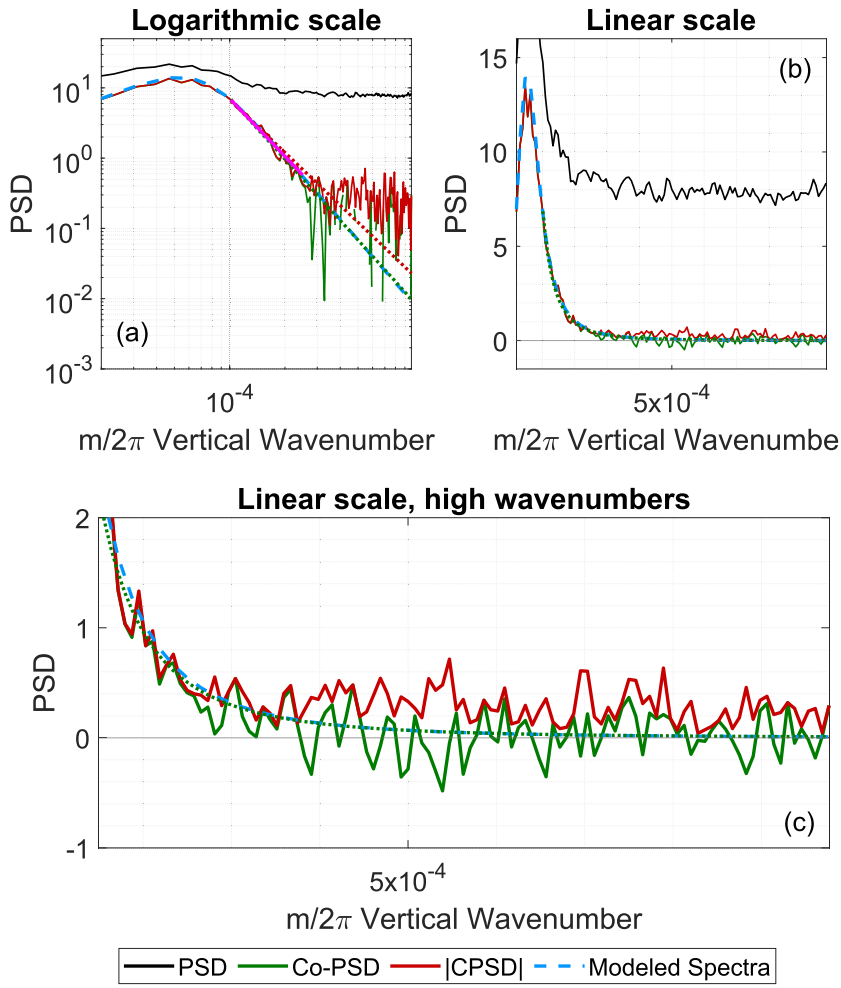

Figure 2. A demonstration of the two CPSD products, Co-PSD and |CPSD|, where 600 samples of the model were used for this plot (see Section 2.4). The plots show that both methods reduce the noise floor from the PSD (black line), but the |CPSD| has a reduced positive bias on it due to the nature of taking the absolute magnitude. The Co-PSD shows negative points; however, this noisy profile is centered on the modeled spectra thus the dashed-green fit line reasonably approximates the modeled spectra. Figures 2b and 2c show the same data, where 2c is zoomed in on the higher m range. Figure 2a shows three fit lines, the green-dashed line is fit to the Co-PSD and the red-dashed line is fit to the |CPSD| over the same range, showing a shallower slope. The pink line in 2a shows the range over which a slope could reasonably be fit to the |CPSD|, which is much smaller than the range of Co-PSD fitting.

negative and positive, this noise term causes only oscillations around the true values of wave spectra, not a bias, and thus a line fit to the Co-PSD profile should reasonably approximate/estimate the wave spectra. We show an example in Figure 2 to demonstrate the ideas stated above (The results of Figure 2 come from a forward model which will be described later in Section 2.4.). Because the Co-PSD (solid green curve) shows both positive and negative values in the linear scale plot (Figures 2b and 2c) when approaching high wavenumbers, a line fitting to the Co-PSD delineates an estimate of the power spectral density (dotted green curve) that closely resembles the forward-modeled true wave PSD (dashed cyan curve).

In comparison, the absolute magnitude of CPSD (|*CPSD*|, red curve) stays positive at all wavenumbers and shows a reduced noise floor above the true wave PSD, which is obvious at high wavenumbers. This reduced noise floor (solid red curve), although being much smaller than the original PSD noise floor (black curve), can still mislead the extraction of the spectral slope over a large range of wavenumbers (dotted red line) or limit the slope extraction to a much-narrower range (solid pink line) above the reduced noise floor in the log-scale plot (Figure 2a). In stark contrast, the Co-PSD slope (dotted green line) follows the modeled spectral slope nicely throughout the high wavenumber range (limited by the Nyquist criterion). This Co-PSD slope is obtained from the

aforementioned fitting in the linear scale (Figures 2b and 2c). The stunning results in Figure 2a are not surprising because taking the CPSD magnitude constitutes a loss of information about part of the spectra, for example, the negative ΔCo and ΔQ, leading to a reduced but non-zero bias as discussed above using Equation 10a. This reduced bias may be understood through an analogy of fluctuations Δx around a mean $\bar{x}$ when taking the square operation: $\sqrt{\frac{(\bar{x}+\Delta x)^2+(\bar{x}-\Delta x)^2}{2}} = \sqrt{(\bar{x})^2+(\Delta x)^2}$. The Co-PSD eliminates the noise floor entirely as shown in Figure 2 because it avoids the operation of taking squares, allowing the negative and positive noise to cancel out each other thus revealing the true spectral slope. However, this complete elimination of spectral noise floor by taking the Co-PSD comes with a drawback—the energy in the neglected Q-PSD imposes a correction factor of Co-PSD from the true wave PSD, and the correction magnitude depends on the shift between two subsamples. Furthermore, because of the splitting in photon counts, the interleaved techniques suffer larger uncertainties than the original PSD. Both points will be addressed in Section 2.3.

2.3. Accuracy and Precision Assessments for Interleaved Methods

An important distinction here is that, inherently, the results of Equations 7a and 7b are bias-free and contain no noise bias/no noise floor but suffer a higher level of uncertainty than a non-interleaved approach due to the split of photon counts. On this sense of bias versus uncertainty, are accuracy and precision defined as two different concepts. The accuracy refers to biases caused by systematic errors, that is, how close the experimental results are to the true values, while the precision refers to uncertainties caused by random errors, that is, how well the results have been determined, without reference to its agreement with the true values (e.g., Bevington & Robinson, 2003; Taylor, 1997—referring to Figures 4.1 and 4.2 of that book; Bendat & Piersol, 2010—referring to Figure 1.18 of that book). Of course, the more independent samples which are averaged, the further that the cross-terms in the interleaved techniques are driven to zero and the uncertainties in the interleaved products are decreased. Incorporating sufficient data to achieve a higher precision will help reveal the high accuracy of the interleaved methods.

2.3.1. Accuracy Assessment

In the very ideal case, for example, simultaneous and common-volume observations made with two lidars provide two independent measurements with zero shift ($\delta z = 0$ and $\delta t = 0$), the Q-PSD is zero, that is, $Q = 0$; therefore, the $Co\text{-}PSD = Co + \Delta Co = PSD_{Wave} + \Delta Co$. That is, the Co-PSD under this ideal case will represent the full PSD induced by waves (still with uncertainties). However, with a single lidar using the interleaved data processing technique to provide two independent measurements, there is always a finite shift ($\delta z \neq 0$ or $\delta t \neq 0$). Even when $L \to \infty$, $\Delta Co \to 0$ so $Co\text{-}PSD \to Co$, the $Co\text{-}PSD$ obtained from the interleaved method will statistically underestimate PSD due to the finite shift δz or δt between the two subsamples, which introduces non-zero Q-PSD. Thus, it is necessary to assess the offset between the Co-PSD of the two subsamples and the true wave-induced PSD of the total samples, that is, to assess the accuracy of Co-PSD. When considering the PSD as calculated in Equation 4, the purely wave-induced perturbations $|DFT(\rho')|^2 = DFT(\rho')\,DFT^*(\rho')$, like the first term on the RHS of Equation 2b, will perfectly auto-correlate with itself, yielding the full energy of the waves. When calculating the Co-PSD as in Equation 7b, the phase shift between two interleaved samples results in the ideal Co-PSD (i.e., the purely wave-induced $Re\left[DFT(\rho'_A)\,DFT^*(\rho'_B)\right] \leq |DFT(\rho')|^2$) underestimating the true energy in the waves being measured, just as with the covariance derived in Gardner and Chu (2020).

We follow the procedure in Bendat and Piersol (2010) to derive the correction term for the Co-PSD from the definition of a time/space shifted Fourier transform (Bendat & Piersol, 2010; von Storch & Zwiers, 1999). Because the two interleaved subsamples can be regarded as identical series which are shifted by δt or δz, we have:

$$F[x(t)] = X(\omega) = \int_{-\infty}^{\infty} x(t)\, e^{-i\omega t} dt \tag{11a}$$

$$F[y(t) \equiv x(t-\delta t)] = Y(\omega) = \int_{-\infty}^{\infty} x(t-\delta t)\, e^{-i\omega t} dt = e^{-i\omega\delta t} \int_{-\infty}^{\infty} x(u)\, e^{-i\omega u} du = e^{-i\omega\delta t} X(\omega) \tag{11b}$$

$$PSD_{xx}(\omega) = \langle X(\omega)\, X(\omega)^* \rangle,\ CPSD_{xy}(\omega) = \langle X(\omega)\, Y(\omega)^* \rangle = e^{i\omega\delta t} PSD_{xx}(\omega) \tag{11c}$$

$$PSD_{xx}(m) = \langle X(m)\,X(m)^{*}\rangle,\ CPSD_{xy}(m) = \langle X(m)\,Y(m)^{*}\rangle = e^{im\delta z}PSD_{xx}(m) \tag{11d}$$

where $F[x(t)]$ is the Fourier transform of $x(t)$ and ω is angular frequency. The angle brackets in Equations 11c and 11d represent the expectations, that is, taking the ensemble averages. We are interested in finding the percentage by which Co-PSD underestimates, so we solve for the correction as

$$\frac{PSD_{wave}(\omega) - Co\text{-}PSD(\omega)}{PSD_{wave}(\omega)} = \frac{PSD_{wave}(\omega) - Re[CPSD(\omega)]}{PSD_{wave}(\omega)} = 1 - Re\left(e^{i\omega\delta t}\right) = 1 - \cos(\omega\delta t) \tag{12a}$$

$$\frac{PSD_{wave}(m) - Co\text{-}PSD(m)}{PSD_{wave}(m)} = \frac{PSD_{wave}(m) - Re[CPSD(m)]}{PSD_{wave}(m)} = 1 - Re\left(e^{im\delta z}\right) = 1 - \cos(m\delta z) \tag{12b}$$

where PSD_{wave} denotes the purely wave-induced power spectral density. Equations 11d and 12b are derived for spatial spectra by substituting ω and δt in Equations 11c and 12a with m and δz. It is worth noting that the correction factors are frequency or wavenumber dependent; that is, under the same shift δt or δz, lower frequency or wavenumber waves will experience smaller correction factors than waves with higher frequencies or wavenumbers. Such a result is expected because the same shift δt or δz comprises a smaller portion of the wave period or vertical wavelength thus introducing smaller phase shift between two interleaved subsamples for waves with longer periods or vertical wavelengths. For example, the University of Colorado Na Doppler lidar has its raw photon count data acquired at resolutions of $\delta t = 4.5$ s and $\delta z = 24$ m, and then data are processed using a time interleaved method, so the time shift is small $\delta t = 4.5$ s (Chu et al., 2020, 2022; Gardner & Chu, 2020). The correction term, given by Equation 12a, is ∼0.44% for waves at the buoyancy frequency (nearly the highest frequency for gravity waves with the corresponding period of ∼5 min) and ∼0.003% for waves with a period of an hour. The Fe Boltzmann lidar used in this study has its raw data taken at $\delta t = 1$ min and $\delta z = 48$ m and then processed using an altitude interleaved method, so the spatial shift $\delta z = 48$ m (Chu et al., 2011a, 2011b; Jandreau & Chu, 2022). The correction term, given by Equation 12b, is ∼4.5%, ∼1.1%, ∼0.18%, and ∼0.01% for waves with vertical wavelengths of 1, 2, 5, and 20 km, respectively. In both examples, the correction factors are negligibly small except for the 1-km waves with a 48-m shift (nearly 5%). It is clear from the demonstrations above that waves with the highest frequencies or wavenumbers suffer the largest correction factors; therefore, the subsamples should be interleaved as closely as possible to maintain coherence in the wave terms between the two subsamples and minimize the correction factors. We may understand Equation 12 as multiplying the true wave PSD with a filter function which attenuates the high frequencies and wavenumbers the most. Equations 12a and 12b can be used to compensate the higher frequency and wavenumber spectra for such attenuation, or to design the data acquisition by choosing δt or δz sufficiently small so that the attenuation is negligible.

It is worth pointing out that the only way to eliminate $(\Delta Co)^2 + (\Delta Q)^2$ biases from the CPSD magnitude is to average over infinite number of independent samples. When $L \to \infty$, $\Delta Co = 0$ and $\Delta Q = 0$ in Equation 10a. Consequently, the expectation of the CPSD magnitude

$$\langle |CPSD| \rangle = \sqrt{Co^2 + Q^2} = \langle PSD \rangle, \quad at\ \Delta Co = 0\ and\ \Delta Q = 0 \tag{13}$$

Interestingly, with no noise, the CPSD magnitude would always equal the PSD, regardless of the shift between the two interleaved subsamples; therefore, the inaccuracy would be zero. This is an interesting aspect of spectral analysis that is different from the computations of variances and fluxes in time or spatial domain. That is, the energy that goes into the Q-PSD due to the shift between two subsamples can be recovered via taking the CPSD magnitude in the spectral domain if the data is noise-free ($\Delta Co = 0$ and $\Delta Q = 0$). Indeed, this unique feature of spectral analysis may be a way to fully recover the variance from covariance, that is, Fourier transform the covariance to the spectral domain and recover the full energy from the real AND imaginary portions of CPSD, and then inverse Fourier transform back to the time-spatial domain to recover the variance consisting of the full wave energy. However, with noise, the reduced noise floor $(\Delta Co)^2 + (\Delta Q)^2$ remains in the CPSD magnitude, making the Co-PSD a more viable approach for deriving noise-floor-free spectra.

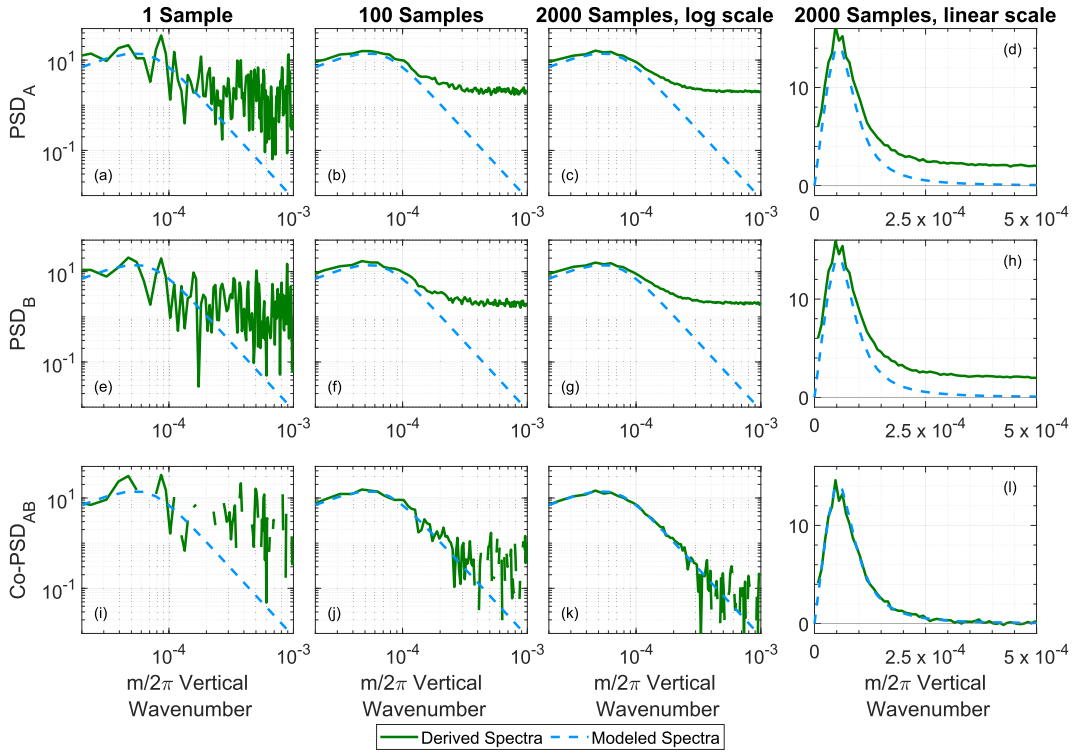

Figure 3. A forward model showcases the interleaved method's convergence toward the modeled spectra with the incorporation of additional samples. The power units here are arbitrary, but the *x*-axis is that of vertical wavenumber and the spectra was scaled to resemble the real data. The first and second rows show the PSD of the subsamples A and B, respectively, and the third row shows the Co-PSD of the two subsamples. The column title designates the number of simulated spectra which were averaged together to generate the displayed plot.

2.3.2. Precision Assessment

While this method of Co-PSD calculation can yield negative values, unlike negative values derived from the calculative subtraction method in Section 2.1, these negative values are simply due to uncertainties which will be driven toward zero with the incorporation of sufficient samples (e.g., a longer time/spatial series, or the incorporation of more observations, or both). Therefore, the interleaved method is viable in conditions where the calculative subtraction method fails. Additionally, this uncertainty should be centered on the true spectra, so even with a noisy Co-PSD, trends and slopes can still be inferred from its profile as demonstrated in Section 2.2 (Figure 2). Uncertainty caused by the cross terms seen in Equations 7 and 8 are driven toward zero as more samples are incorporated because the noise terms are independent of the wave signals and of each other and are thus uncorrelated. Again, these cross terms will only truly become zero in the case of an infinite-length signal, but the averaging of additional samples allows these cross-terms to approach zero. Given the inherently less precise (but more accurate) nature of the interleaved method caused by the split of photon counts, it is worth quantitatively considering the number of samples which must be averaged together to achieve a desired uncertainty. This is obviously related to the SNR of the signal, where higher noise will require more samples to defeat. In Equation 14, we provide a relation to determine the number (N) of independent samples which must be averaged together to reduce the uncertainty contributed by the cross terms to a desired amount $\left(\Delta\rho/\rho'\right)_{desired}$:

$$N \geq \left(\frac{2\Delta\rho/\rho'}{\left(\Delta\rho/\rho'\right)_{desired}}\right)^2 \tag{14}$$

where the ratio $\Delta\rho/\rho'$ is a representative ratio of a density error estimate to the density perturbation strength for a single full sample (on the statistical sense). Here $\Delta\rho$ refers to a full sample error, while the interleaved subsample error $|\Delta\rho_A| = |\Delta\rho_B| = \sqrt{2}|\Delta\rho|$ statistically due to the splitting of photon counts. Equation 14 is derived by taking

10.1029/2023EA003499

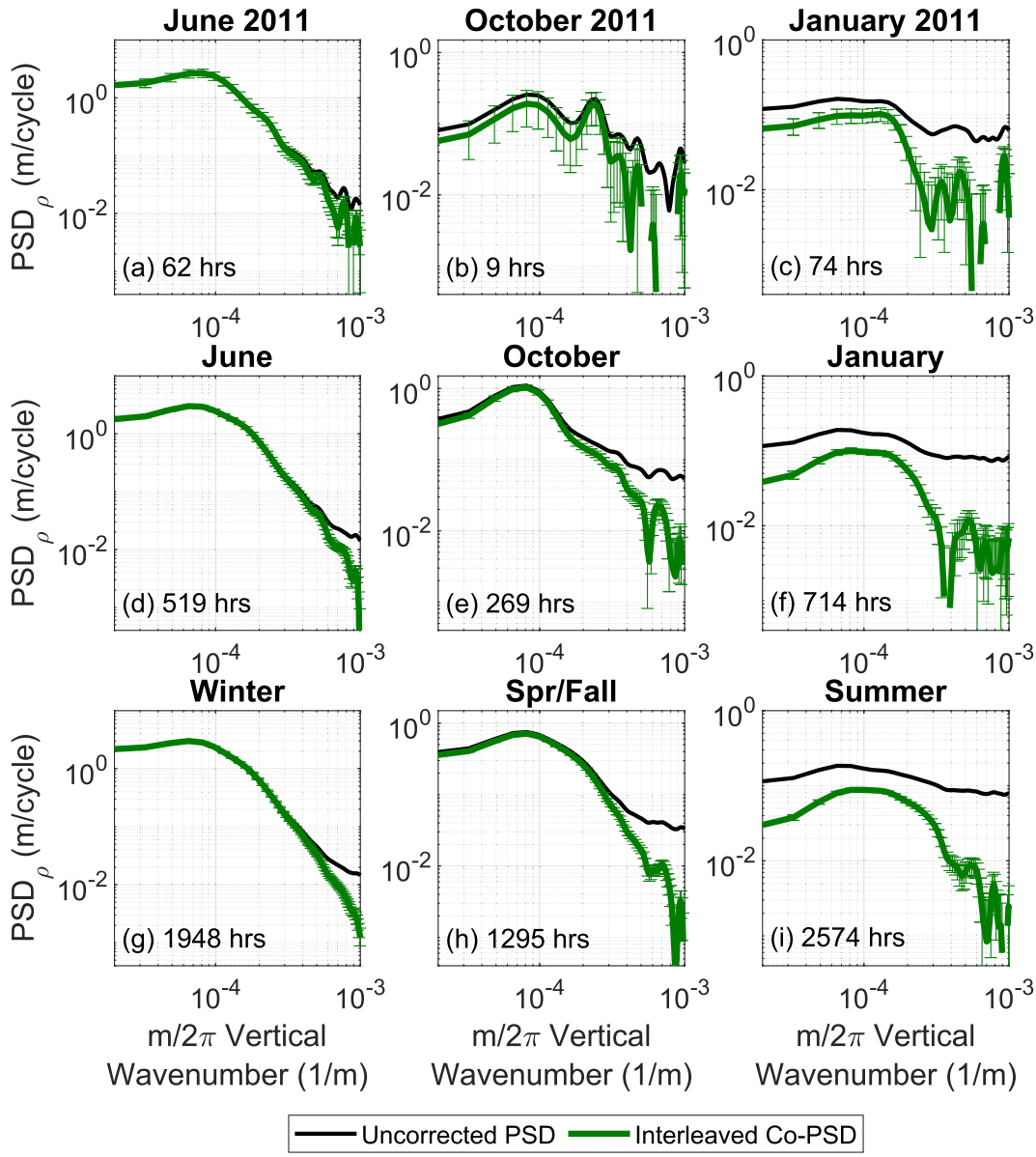

Figure 4. 10-year average vertical wavenumber ($m/2\pi$) spectra from 30 to 50 km derived from atmospheric density using data at a resolution of 1 hr and 0.48 km. See text for details about lines plotted. On the third row, Winter includes May, June, July, and August; Spring/Fall includes September, October, March, and April; Summer includes November, December, January, and February. The hour number in each plot denotes the amount of data used in the sample average for each plot.

the ratio of the three cross-terms in Equation 7a to the wave term $\rho'_A\rho'_B$ and approximating the relation to the first order. For example, in our winter data at resolutions of 1 hr and 0.5 km, looking at an altitude of 45 km, we often see a ratio of $\Delta\rho/\rho' = 0.2$–0.4, which means that we must accumulate ∼16–64 independent samples to achieve a desired error $\left(\Delta\rho/\rho'\right)_{desired} \approx 10\%$ or ∼64–256 samples for reducing to 5% desired error. For summer data taken under full sunlight, where $\Delta\rho/\rho'$ can be as large as 0.75–1.25, we must acquire ∼225–625 independent samples to reduce the cross-term uncertainty contribution to 10%. Due to the linearity of the Fourier transform, these approximations should hold similarly true for the cross-terms of Co-PSD and CPSD magnitude in Equations 7b and 7c. Based on these approximated ratios, the summer cross-term reduction seen in Figure 4 (Section 3) using ∼2,500 samples of lidar observations in Antarctica is down to about ∼5% of the wave amplitude.

More comprehensive assessment of the measurement precision requires the derivations of spectral uncertainties caused by the random errors, which must systematically consider both the statistical errors and the photon-noise-

induced errors. Uncertainties caused by the cross terms discussed above represent the photon-noise-induced errors, which could dominate data with low signal-to-noise ratios (SNRs), for example, the daytime or summer lidar data in polar regions under the full sunlight or near the edges of atmospheric layers (like the upper portion of Rayleigh scattering or the bottom and top edges of metal layers in the MLT) where photon noise can be significant (e.g., $\Delta\rho/\rho' \sim 1$ or higher). However, even in an ideal case where the photon noise is minimal, like nighttime or winter lidar data in polar region under dark skies or near the peak of atmospheric layers, or in an extreme case of zero instrumental errors ($\Delta\rho = \Delta\rho_A = \Delta\rho_B = 0$) so that the cross terms vanish, there are still uncertainties to the measured Co-PSD and PSD, which are caused by the statistical errors (Bendat & Piersol, 2010; Gardner & Yang, 1998). Statistical errors are uncertainties that stem from the inability of a finite number/length of samples to fully estimate the measured variable of a random process. For relatively high SNR data, the spectral uncertainties are usually dominated by the statistical errors, not photon noise, because the correlation time τ_C of the ρ' or T' spectra is usually longer than the correlation time of photon noise. The correlation time (also sometimes called the decorrelation time) is the length of time over which a signal self-correlates to a significant degree. The photon noise of every bin is uncorrelated to the next or other bins; thus, the photon noise correlation time equals the observation resolution Δt. Under the same observational time τ_{obs}, the numbers of statistically independent samples are $n_d = \tau_{obs}/\tau_C$ and $n_p = \tau_{obs}/\Delta t$ for the statistical errors and for the photon-noise-induced errors, respectively. When $\tau_C \gg \Delta t$, $n_d \ll n_p$ so the statistical error reduction is much slower than the photon-noise error reduction.

Appendix A provides a detailed procedure of the derivations of spectral uncertainty equations for the Co-PSD and PSD, along with the computation of correlation times. Our derivations are based on the book "Random Data" by Bendat and Piersol (2010). The approaches in their Chapter 9 of "Statistical Errors in Advanced Estimates" are adopted and modified to derive the spectral uncertainties introduced by random errors that include both the statistical error and instrumental noise. The uncertainties for the m-spectral Co-PSD and PSD are given as

$$\Delta\overline{Co\text{-}PSD}(m) = \sqrt{\frac{\tau_C}{\tau_{obs}} Co\text{-}PSD^2_{\rho'_{A,total}\rho'_{B,total}}(m) - \frac{\tau_C}{2\tau_{obs}} Q^2_{\rho'_{A,total}\rho'_{B,total}}(m) + \frac{\Delta t}{\tau_{obs}} Co\text{-}PSD_{\rho'_{A,total}\rho'_{B,total}}(m)\, PSD_{\Delta\rho_{int}}(m) + \frac{\Delta t}{2\tau_{obs}} PSD^2_{\Delta\rho_{int}}(m)} \tag{15a}$$

$$\Delta\overline{PSD}(m) = \sqrt{\frac{\tau_C}{\tau_{obs}} Co\text{-}PSD^2_{\rho'_{A,total}\rho'_{B,total}}(m) + \frac{2\Delta t}{\tau_{obs}} Co\text{-}PSD_{\rho'_{A,total}\rho'_{B,total}}(m)\, PSD_{\Delta\rho}(m) + \frac{\Delta t}{\tau_{obs}} PSD^2_{\Delta\rho}(m)} \tag{15b}$$

where the uncertainty $\Delta\rho_{int}$ (which represents $\Delta\rho_A$ or $\Delta\rho_B$) of interleaved ρ'_A and ρ'_B is larger than the uncertainty $\Delta\rho$ of non-interleaved ρ', $\langle|\Delta\rho_{int}|\rangle = \sqrt{2}\langle|\Delta\rho|\rangle$, due to the photon count split. Consequently, $PSD_{\Delta\rho_{int}} = 2PSD_{\Delta\rho}$. Here $PSD_{\Delta\rho}$ can be calculated as $PSD_{\Delta\rho} = PSD_{\rho'_{total}} - Co\text{-}PSD_{\rho'_{A,total}\rho'_{B,total}}$. More details can be found in Appendix A. From Equation 15, the reduction of the statistical error goes by $\sqrt{1/n_d}$; therefore, at least $n_d \sim 25$ is needed to drive the spectral uncertainty to ~20% of Co-PSD. As shown in Appendix A, the correlation time for ρ' spectrum measured by lidar is about 1–2 hr. Consequently, at least 25–50 hr of lidar measurements are required. As lidar observational window length is usually around 8–25 hr at McMurdo, beating down the statistical error requires at least 2–7 different observation periods. Certainly, for low SNR data as mentioned above, the reduction of spectral uncertainties also requires beating down the photon noise. This is especially true in the high wavenumber or frequency regime where the power spectral density decreases nearly exponentially, so photon noise makes significant contributions to the spectrum uncertainties, which require more samples to reduce.

2.4. Forward Modeling to Demonstrate Interleaved Method

The derivation of an unbiased spectrum via the interleaved method and the reduction of uncertainty through the incorporation of additional samples is demonstrated through a simple forward model shown in Figures 2 and 3. The model spectrum used here is based on a spectrum commonly adopted for vertical wavenumbers in the ocean and atmosphere (Desaubies, 1976; Senft & Gardner, 1991; Smith, 1987; Van Zandt, 1982):

$$F(m) = \frac{F_0\left(\frac{m}{m^*}\right)^s}{1 + \left(\frac{m}{m^*}\right)^{(3+s)}} \quad (16)$$

where F_0 is a scaling constant, m is the vertical wavenumber, m^* is the characteristic wavenumber, s is a source-dependent parameter for which $s = 1$ is a typical assumption for these types of waves (Senft & Gardner, 1991). A key part of this model is that the spectra at high-m values ($m > m^*$) is proportional to m^{-3}, as indicated by the three in the denominator. This model generally reflects the average behavior of the gravity waves observed in the McMurdo lidar campaign. The modeling procedure follows that of Tsuda et al. (1989) and Owens (1978) where the desired spectra are given a random $0-2\pi$ phase shift and transformed to a 1-D spatial series using an inverse-Fourier transform. The phase shift allows the generation of many unique spatial series which share the same underlying spectra to which random, zero-mean Gaussian noise is added. In this model, we split the noisy spatial series into two subsamples, A and B, in an interleaved fashion via Section 2.2 and bin the series to replicate the binning of the real data. We then use Equation 4 to calculate the PSD of subsample A and subsample B, but we also calculate the Co-PSD of the two subsamples via Equation 7b. The two PSDs are plotted in the first two rows of Figure 3 and the Co-PSD is plotted in the third row. Column 4 displays the same data as column 3 but on a linear scale to emphasize the noise floor. Figure 3 demonstrates how the PSD and Co-PSD values respond to various sample sizes, clearly showing how additional samples evolve the noise floor in the PSD while showing there is no noise floor in the Co-PSD. It is also clear from the third row that the Co-PSD has increased uncertainty levels and, with the lower sample sizes of column 1 and 2, has many negative points. Because negative values cannot be shown in the log-scale plots of panels (i) and (j), these positive-only log-scale plots are somewhat misleading. Once plotted in the linear scale, it is clear that the Co-PSD fluctuates/oscillates with both negative and positive values around the true (modeled) wave spectra, similar to the demonstration in Figures 2b and 2c. As the large uncertainties and negative bins of Co-PSD induced by statistical and photon noise are minimized with the incorporation of additional samples, the Co-PSD converges toward the modeled spectra (Figures 3k and 3l). This same model was also used to generate Figure 2 and compare the two CPSD products (i.e., $|CPSD|$ and Co-PSD).

3. Demonstration Using McMurdo Lidar Observations and Data Handling Details

The University of Colorado lidar group has been running an Fe Boltzmann lidar from Arrival Heights Observatory (77.84°S, 166.67°E) near McMurdo, Antarctica since Dec 2010 via collaboration between the United States Antarctic Program and Antarctica New Zealand (Chu et al., 2011a, 2011b). Operating at 372 and 374 nm, this lidar measures the atmospheric density and temperature from 30 up to ~70 km via Rayleigh lidar techniques (e.g., Chu et al., 2002) and the meteoric Fe-layer density and temperature above 70 km to the thermosphere via the resonance fluorescence and Boltzmann techniques (Chu, Yu, et al., 2011; Chu & Papen, 2005; Gelbwachs, 1994). The measurement ranges, resolutions, and precisions largely depend on the operation conditions (Chu et al., 2002), for example, nighttime versus daytime, with the nighttime data extended into much larger detection ranges and higher resolutions/precisions than those of the daytime (Chu et al., 2011a, 2011b, 2020; Chen et al., 2016; Zhao et al., 2017; Li et al., 2020). The raw photon counts were collected in resolutions of 48 m and 1 min in both channels. The 10 years of the 374-nm channel Rayleigh scattering data from Dec 2010 through Oct 2020 are used in this study for demonstration of the interleaved data processing techniques in the gravity wave spectral analyses.

3.1. Data Handling and Processing Details

Antarctic winter/summer experiences full darkness/full daylight, while spring and fall go through day-night transitions at McMurdo. Because of the solar background variations, the SNRs of lidar data are in general highest and lowest in winter and summer, respectively, and medium in spring and fall. To compare the effectiveness of the three methods on noise floor corrections, we choose June, October, and January to represent the highest (winter), medium (spring and fall), and lowest (summer) SNR cases in this study. Over the 10-year data collection period, extensive good data were collected in June in nine of the 10 years (except June 2018 due to bad weather) and in October and January in all 10 years. Our definitions of seasons are that winter includes May, June, July, and August; spring/fall includes September, October, March, and April; summer includes November, December, January, and February.

We limit this comparison to the altitude range of 30–50 km so that performance of the methods on the winter and summer data can be directly compared (some daytime data cannot be reliably retrieved above 50 km). The resolutions utilized here are 1 hr time bins and 0.48 km altitude bins. These bins were selected to provide a good balance of SNR, while still extending far enough into the high-wavenumber range to demonstrate the noise floor methods well. The relative wave perturbations were calculated from atmospheric density by subtracting the time-averaged density-profile from the array at each altitude, dividing the density perturbation field by that profile, and then subtracting the vertical-mean perturbation profile to remove spatial trends due to the long-wavelength waves such as tides and planetary waves.

Great care should be taken to ensure that the PSDs calculated are not affected by specifics of the spectral processing to allow comparison with theoretical spectral models and other measurements. The PSDs shown are calculated by zero-padding the spatial series to a length of 128 points. Before padding, the data series is multiplied by a Hann-window in order to reduce spectral leakage in the high-wavenumber amplitudes (Blackman & Tukey, 1958). The final PSD and Co-PSD are then calculated as in Equation 4 and 7b, and to undo the power loss due to the windowing process, the PSD/Co-PSD is divided by the square of the mean of the window function. The calculation of the PSDs must be done properly such that the zero-padding does not affect the derived power of waves, which is given by the integrated area below the PSD envelope. The proper approach is to scale the PSDs from the DFT square using the unpadded number of data points as in Equation 4, instead of scaling by the padded number.

The spectra are compared on three levels: A single month, an average of 10 months, and a seasonal average (~40 months). All averages are weighted by observation lengths. Using the Co-PSD given in Equation 7b as we do here in Figure 4, the Co-PSD can be averaged together and the cross-term induced uncertainties will continue to decrease. If one were to use the $|CPSD|$ as in Equation 7c, the results with the minimum bias would result from averaging as much data together as possible before taking the absolute magnitude to allow for the maximum cross-term reduction. To facilitate the demonstration of the interleaved techniques, the comparison of two conventional noise-floor-removal methods with the interleaved method is given in Appendix B. The graphical inspection method is uniquely sensitive to the spectra which is "inspected." As additional spectra are averaged together, the uncertainty in the resultant spectrum decreases and becomes smoother, making it easier for the floor-finding algorithm to identify the floor. For this reason, in each subplot of Figure B1, the graphical inspection method is applied to the uncorrected spectra at that level of averaging, as this practice ensures the algorithm had the best chance of finding the proper floor. The calculative noise-subtraction method is not sensitive to application order (subtracting the floor of individual observations has similar effectiveness as averaging many observations and their individual noise floors and then subtracting this floor) as long as the averaging is handled properly.

3.2. Results of Spectral Interleaving

In Figure 4, the results from the interleaved method are plotted against the uncorrected spectrum for vertical wavenumber calculations in three scenarios (winter, spring/fall, and summer representing three different levels of data SNRs), each with a different amount of data (a single month, 10 months, and 10 seasons) included in the average in order to demonstrate the effect of incorporating more data. The interleaved Co-PSD shows multiple instances of negative power in Figures 4b and 4c where the sample size is small and the inflated uncertainties inherent to the method have yet to be defeated. Section 2.2 demonstrates that while these negative points should still be centered on the wave spectrum, it is difficult to visually assess the spectrum with the negative points present. The larger sample sizes for the spring/fall and summer results show great improvement compared to Figures 4b and 4c due to the larger sample size. This Co-PSD, for the reasons discussed in Section 2.2 and 2.3, should be the most accurate of the three methods introduced in Section 2.1, though its precision may be lower than the other methods under certain conditions.

In Figure 5, we demonstrate $\Delta Co\text{-}PSD_{\rho'_{A,total}\rho'_{B,total}}$ and $\Delta PSD_{\rho'_{tot}}$. The uncertainties are calculated via Equations 15a and 15b where a correlation time of $\tau_C \cong 1.7$ hr is used for the density perturbations (estimation of correlation time is provided in Appendix A).

4. Conclusions and Recommendations

Based on the original proposal by Gardner and Chu (2020), we have investigated the interleaved data processing techniques for spectral analysis of atmospheric waves through theoretical studies, forward modeling, and

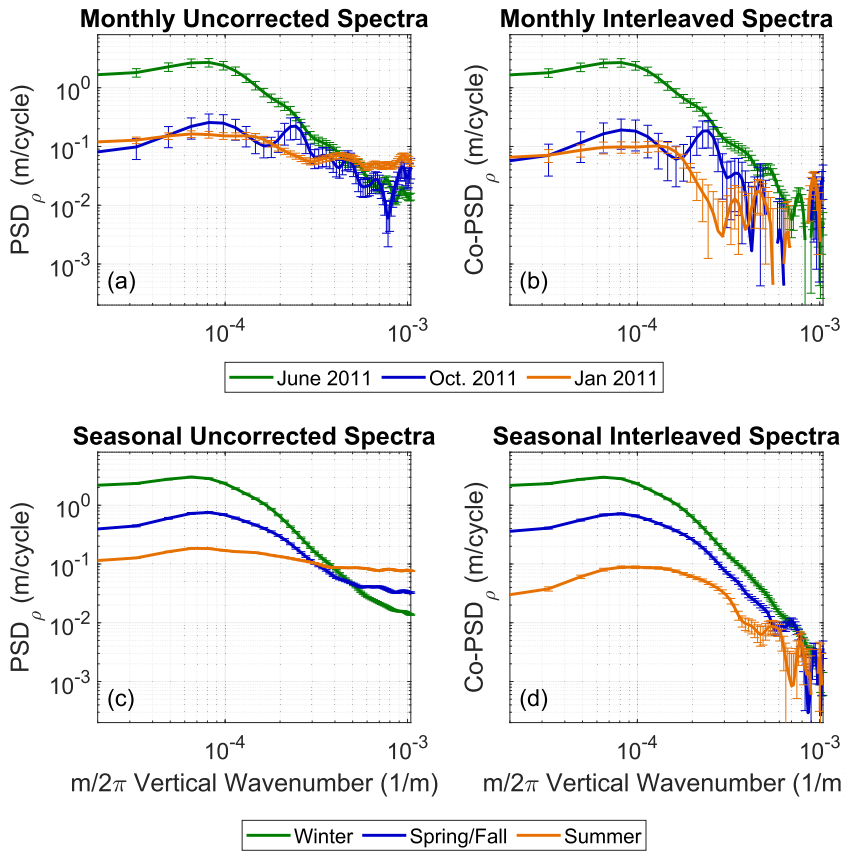

Figure 5. Demonstration of the uncertainty calculation of the vertical wavenumber ($m/2\pi$) spectra of each season. The top row shows one month of data, while the lower row shows the 10-year seasonal means. This figure shows both the increase in error of the interleaved method, but also the decreasing uncertainty as additional samples are incorporated. It should be noted that in the logarithmic scale of the y-axis, negative values cannot be plotted thus some points are omitted from Figure 5b.

demonstration with lidar observational data from Antarctica as well as through comparison to two existing noise-subtraction methods. Our results have clearly demonstrated that calculating the cross-power spectral density (CPSD) from two interleaved subsamples does reduce the spectral noise floor significantly. However, only the Co-PSD, that is, taking the real part of CPSD, eliminates the noise floor completely, while the method of taking the CPSD magnitude adds a reduced noise floor back to the power spectral density when the number of samples is finite. The reason is that the Co-PSD does not take any absolute magnitude or square, avoiding loss of the information on the negative and positive signs of noise-induced ΔCo and ΔQ. However, a drawback of taking the Co-PSD is the slight loss of energy induced by the non-zero imaginary part of CPSD, that is, the Q-PSD, which is caused by the non-zero shift (δz or δt) between two subsamples. Accuracy assessment has shown that the correction term of Co-PSD from the purely wave-induced PSD is wavenumber or frequency dependent, with higher wavenumber or frequency waves suffering larger energy loss. Such correction term can be minimized by minimizing the shift between two interleaved subsamples. In an ideal situation of simultaneous and common-volume observations using two lidars, the shift between two independent samples (now from two independent lidars) can be made zero ($\delta z = 0$ and $\delta t = 0$), then $Q\text{-}PSD = 0$, that is, the Co-PSD does not have energy loss anymore while the noise floor is still eliminated completely. This is because the noise terms from two independent lidar samples are uncorrelated, and they are also uncorrelated to the wave perturbations.

Although a reduced noise floor is inherent to the method of taking the magnitude of sample averaged CPSD, this noise floor can be further minimized through averaging over more observations. This situation is completely different from the traditional PSD calculations whose noise floor cannot be reduced by incorporating more samples. Additionally, the CPSD magnitude contains the full wave energy (with reduced noise power as well) regardless the shift between two interleaved subsamples. For instance, if the shift corresponds to an exact 90-deg phase shift, the $Co\text{-}PSD = 0$ but the Q-PSD carries the full wave energy, so the CPSD magnitude still contains the

full wave energy. Indeed, this unique feature of cross-spectrum may be a way to fully recover wave-induced variance from covariance, that is, Fourier transform the covariance to the spectral domain and recover the full energy from the real and imaginary portions of cross-spectrum, and then inverse Fourier transform back to the time-spatial domain to recover the variance consisting of the full wave energy. This suggestion is beyond the scope of this study but deserves a future study.

Both the CPSD magnitude and Co-PSD methods of the interleaved data processing techniques experience larger photon-noise-induced uncertainties than the traditional noise-floor-subtraction methods, due to the split of photon counts during the interleaving process. We have provided a comprehensive assessment of the measurement precision that details the derivations of spectral uncertainties caused by random errors. Our derivations of uncertainty equations are based on the book "Random Data" by Bendat and Piersol (2010) but we modify their approach to derive the spectral uncertainties introduced by both the statistical error and photon noise. The number of statistically independent samples and observational time length required to reduce the spectral uncertainties are determined from these equations.

Overall, our recommendations to users are as follows. If the noise-floor-free spectra are the top requirement under finite number of samples, the Co-PSD interleaved method is the preferred approach; but if a reduced noise floor is acceptable, especially in the case of large sample shift δz or δt, the method of taking the CPSD magnitude is still a good approach. Users can assess their required accuracy and precision along with their data conditions (like the minimum achievable δz or δt and the number of samples) to determine the best choice for their applications. It is worth noting that an inherent problem associated with noise-floor-subtraction methods is that it is impossible to know errors exactly (otherwise, they were no longer errors as we could subtract the "exact" errors from measurements and obtain accurate results without errors). The spectral interleaved technique is a significant advancement over the traditional noise-floor-subtraction methods because it does not rely on an accurate estimate of the error to subtract the noise-floor from the spectra as do the pre-existing methods, instead using the statistical properties of the signal and noise to inherently eliminate this noise floor. This feature removes the subjectivity of floor identification and does not rely on assumptions in the noise calculation, improving overall confidence of the results. It is worth noting that computing power spectra from interleaved data is most useful for data exhibiting pink, white, or even blue spectra (such as gravity-wave-induced vertical wind perturbations), where it would be difficult to isolate the noise floor in the computed spectra. While this study showcases the interleaved methods as applied to lidar-observed atmospheric density, the interleaved techniques are readily applicable to a wide variety of observational data sets including lidar, radar, other remote sensing and in-situ observations of the atmosphere and space as well as of other fields.

Appendix A: Derivations of Spectral Uncertainties and Correlation Times

The derivations of spectral uncertainties are based on the book "Random Data" by Bendat and Piersol (2010). The approaches in their Chapter 9 of "Statistical Errors in Advanced Estimates" are adopted and modified to derive the spectral uncertainties introduced by random errors that include both the statistical error and instrumental noise (e.g., photon noise).

A1. Deriving A General Solution of the Co-Spectral Uncertainty of Noisy Signals

We define two data series, which are individual samples of stationary and ergodic random processes, as

$$x_{total}(z, t) = x(z, t) + \Delta x(z, t) \tag{A1a}$$

$$y_{total}(z, t) = y(z, t) + \Delta y(z, t) \tag{A1b}$$

where each term consists of a signal component, x and y, and a noise component, Δx and Δy. Note that t represents time, and z represents altitude of these temporospatial variables and that these signal and noise components are independent Gaussian distributions with zero-mean. We then define the complex spatial DFT of these individual data series as the instantaneous spatial DFTs X_{Total} and Y_{Total}:

$$DFT[x_{total}(z, t)] = X_{Total}(m, t) = X_R(m, t) + X_{\Delta R}(m, t) + i[X_I(m, t) + X_{\Delta I}(m, t)\,] \tag{A2a}$$

$$DFT\left[y_{total}(z,\,t)\right] = Y_{Total}(m,\,t) = Y_R(m,\,t) + Y_{\Delta R}(m,\,t) + i[Y_I(m,\,t) + Y_{\Delta I}(m,\,t)\,] \tag{A2b}$$

where the subscriptions R and I as well as ΔR and ΔI denote the real and imaginary components of the signal DFT and noise DFT, respectively. It is critical to note that the indices $(m,\,t)$ of these spectral terms represent spectra calculated from x and y over an altitude (z) range at an instant in time (t) and that future instances of X and Y terms will possess an implied $(m,\,t)$ even if not written as such. Due to the linearity of the DFT, all components in Equation A2 are independent, normally distributed, and zero-mean.

This appendix adopts a different notation system for spectral terms than the main text to simplify the following derivations that contain many terms. We let $\tilde{G}_{xy}(m,t)$ represent the instantaneous CPSD (equivalent to Equation 9a), where the over-tilde denotes an instantaneous spectral sample.

$$\tilde{G}_{x_{total}\,y_{total}}(m,\,t) = \frac{2}{L}[X_{Total}(m,\,t)\,Y^*_{Total}(m,\,t)\,] \tag{A3a}$$

$$\widetilde{Co}_{x_{total}\,y_{total}}(m,\,t) = Re\left[\tilde{G}_{x_{total}\,y_{total}}(m,\,t)\right] = \frac{2}{L}Re[X_{Total}(m,\,t)\,Y^*_{Total}(m,\,t)\,] \tag{A3b}$$

$$\tilde{Q}_{x_{total}\,y_{total}}(m,\,t) = Im\left[\tilde{G}_{x_{total}\,y_{total}}(m,\,t)\right] = \frac{2}{L}Im[X_{Total}(m,\,t)\,Y^*_{Total}(m,\,t)\,] \tag{A3c}$$

$$\tilde{G}_{x_{total}x_{total}}(m,\,t) = \frac{2}{L}[X_{Total}(m,\,t)\,X^*_{Total}(m,\,t)\,] \tag{A3d}$$

where $\tilde{G}_{x_{total}\,y_{total}}$ is an instantaneous observation of the cross-spectrum, $\widetilde{Co}_{x_{total}\,y_{total}}$ is the instantaneous Co-spectrum, $\tilde{Q}_{x_{total}\,y_{total}}$ is the instantaneous Q-spectrum, and $\tilde{G}_{x_{total}x_{total}}$ is an instantaneous auto-spectrum which is a special case of $\tilde{G}_{x_{total}\,y_{total}}$. Again, the label of instantaneous indicates a spatial spectrum at an instant in time. Here, L represents the data length in space of the individual observation which is Fourier transformed, such as $L = 20$ km for a spectrum taken of a lidar profile from 30 to 50 km.

These instantaneous spectra are drawn from a process whose ensemble mean spectrum is G_{xy}. The sample average $\overline{G}_{xy}$ of these instantaneous samples is denoted with an overbar. We use the following definitions:

$$G_{x_{total}\,y_{total}}(m) = \lim_{n_d\to\infty}\frac{1}{n_d}\sum_{k=1}^{n_d}\left[\frac{2}{L}X_{Total}(m,\,t_k)\,Y^*_{Total}(m,\,t_k)\right] \tag{A3e}$$

$$\overline{G}_{x_{total}\,y_{total}}(m) = \frac{1}{n_d}\sum_{k=1}^{n_d}\left[\frac{2}{L}X_{Total}(m,\,t_k)\,Y^*_{Total}(m,\,t_k)\right] \tag{A3f}$$

where the variable n_d denotes the number of statistically independent samples of the spectra being investigated. It is worth noting that the number of independent samples is not necessarily equal to the number of profiles being averaged due to the correlation time of the random process, a concept which is elaborated upon further on in this appendix. For readability in this derivation, all indices like m and t are dropped, and X and Y variables are always instantaneous.

Ultimately, we are interested in calculating the uncertainty of the Co-spectrum and of the auto-spectrum induced by random errors (including both the statistical error and photon-noise-induced error). We use the following definition of the uncertainty, based on the variance, where $\langle\bullet\rangle$ represents an expectation operation:

$$\Delta\widetilde{Co}_{x_{total}\,y_{total}} = \sqrt{Var\left(\widetilde{Co}_{x_{total}\,y_{total}}\right)} \tag{A4a}$$

$$Var\left(\widetilde{Co}_{x_{total}\,y_{total}}\right) = \left\langle\widetilde{Co}^2_{x_{total}\,y_{total}}\right\rangle - \left\langle\widetilde{Co}_{x_{total}\,y_{total}}\right\rangle^2 \tag{A4b}$$

Table A1
Expectations of Nonzero Products of DFT Components

$\langle X_R X_R \rangle = \langle X_I X_I \rangle = \frac{L}{4} G_{xx}$	$\langle X_{\Delta R} X_{\Delta R} \rangle = \langle X_{\Delta I} X_{\Delta I} \rangle = \frac{L}{4} G_{\Delta x \Delta x}$
$\langle Y_R Y_R \rangle = \langle Y_I Y_I \rangle = \frac{L}{4} G_{yy}$	$\langle Y_{\Delta R} Y_{\Delta R} \rangle = \langle Y_{\Delta I} Y_{\Delta I} \rangle = \frac{L}{4} G_{\Delta y \Delta y}$
$\langle X_R Y_R \rangle = \langle X_I Y_I \rangle = \frac{L}{4} Co_{xy}$	$\langle X_R Y_I \rangle = -\langle X_I Y_R \rangle = \frac{L}{4} Q_{xy}$
$\langle X_{\Delta R} Y_{\Delta R} \rangle = \langle X_{\Delta I} Y_{\Delta I} \rangle = \frac{L}{4} Co_{\Delta x \Delta y}$	

Thus, we must solve for the two variance components of Equation A4b to compute the uncertainty. We derive a general form of the variance from which the uncertainties of both the interleaved Co-spectrum and the auto-spectrum can be inferred.

We start by solving for a general solution of $\left\langle \widetilde{Co}_{x_{total}\, y_{total}} \right\rangle^2$. Expanding Equation A3b using Equation A2 yields,

$$\begin{aligned} \widetilde{Co}_{x_{total}\, y_{total}} &= \frac{2}{L} Re(X_{Total}\, Y^*_{Total}) = \frac{2}{L} Re\{[X_R + X_{\Delta R} + i(X_I + X_{\Delta I})]\,[Y_R + Y_{\Delta R} - i(Y_I + Y_{\Delta I})]\} \\ &= \frac{2}{L}(X_R\, Y_R + X_R\, Y_{\Delta R} + X_{\Delta R}\, Y_R + X_{\Delta R}\, Y_{\Delta R} + X_I\, Y_I \; + X_I\, Y_{\Delta I} \; + X_{\Delta I}\, Y_I \; + X_{\Delta I}\, Y_{\Delta I}) \end{aligned} \tag{A5}$$

The expectation operation can be distributed to each term:

$$\left\langle \widetilde{Co}_{x_{total}\, y_{total}} \right\rangle = \frac{2}{L} \begin{bmatrix} \langle X_R\, Y_R \rangle + \langle X_R\, Y_{\Delta R} \rangle + \langle X_{\Delta R}\, Y_R \rangle + \langle X_{\Delta R}\, Y_{\Delta R} \rangle \\ + \langle X_I\, Y_I \rangle + \langle X_I\, Y_{\Delta I} \rangle + \langle X_{\Delta I}\, Y_I \rangle + \langle X_{\Delta I}\, Y_{\Delta I} \rangle \end{bmatrix} \tag{A6}$$

Table A1 defines the expectations of all possible products of these DFT components, which follow from combining Equations A2 and A3. In Table A1, the property that a true random variable (RV) will be equally symmetric and asymmetric results in equal auto-spectra of the real and imaginary components. Any combination of terms not listed in the table has an expectation of zero.

Applying these definitions to Equation A6 yields

$$\left\langle \widetilde{Co}_{x_{total}\, y_{total}} \right\rangle = \frac{2}{L}\left\langle \frac{L}{4} Co_{xy} + \frac{L}{4} Co_{xy} + \frac{L}{4} Co_{\Delta x \Delta y} + \frac{L}{4} Co_{\Delta x \Delta y} \right\rangle = Co_{xy} + Co_{\Delta x \Delta y} \tag{A7}$$

which enables a general solution for the second term of Equation A4b

$$\left\langle \widetilde{Co}_{x_{total}\, y_{total}} \right\rangle^2 = (Co_{xy} + Co_{\Delta x \Delta y})^2 = Co_{xy}^2 + 2 Co_{xy} Co_{\Delta x \Delta y} + Co_{\Delta x \Delta y}^2 \tag{A8}$$

We then solve for a general solution for the first term of Equation A4b, $\left\langle \widetilde{Co}^2_{x_{total}\, y_{total}} \right\rangle$. We expand this using the RHS of A5:

$$\begin{aligned} \left\langle \widetilde{Co}^2_{x_{total}\, y_{total}} \right\rangle &= \frac{4}{L^2} \langle (X_R\, Y_R + X_R\, Y_{\Delta R} + X_{\Delta R}\, Y_R + X_{\Delta R}\, Y_{\Delta R} + X_I\, Y_I + X_I\, Y_{\Delta I} + X_{\Delta I}\, Y_I + X_{\Delta I}\, Y_{\Delta I})^2 \rangle \\ &= \frac{4}{L^2} \left\langle \begin{array}{c} X_R X_R\, Y_R\, Y_R + 2 X_R X_R\, Y_R\, Y_{\Delta R} + X_R X_R\, Y_{\Delta R}\, Y_{\Delta R} + 2 X_R X_{\Delta R}\, Y_R\, Y_R + 4 X_R X_{\Delta R}\, Y_R\, Y_{\Delta R} \\ + 2 X_R X_{\Delta R}\, Y_{\Delta R}\, Y_{\Delta R} + 2 X_R X_I\, Y_R\, Y_I + 2 X_R X_I\, Y_R\, Y_{\Delta I} + 2 X_R X_I\, Y_{\Delta R}\, Y_I + 2 X_R X_I\, Y_{\Delta R}\, Y_{\Delta I} + 2 X_R X_{\Delta I}\, Y_R\, Y_I \\ + 2 X_R X_{\Delta I}\, Y_R\, Y_{\Delta I} + 2 X_R X_{\Delta I}\, Y_{\Delta R}\, Y_I + 2 X_R X_{\Delta I}\, Y_{\Delta R}\, Y_{\Delta I} + X_{\Delta R} X_{\Delta R}\, Y_R\, Y_R + 2 X_{\Delta R} X_{\Delta R}\, Y_R\, Y_{\Delta R} + X_{\Delta R} X_{\Delta R}\, Y_{\Delta R}\, Y_{\Delta R} \\ + 2 X_{\Delta R} X_I\, Y_R\, Y_I + 2 X_{\Delta R} X_I\, Y_R\, Y_{\Delta I} + 2 X_{\Delta R} X_I\, Y_{\Delta R}\, Y_I + 2 X_{\Delta R} X_I\, Y_{\Delta R}\, Y_{\Delta I} + 2 X_{\Delta R} X_{\Delta I}\, Y_R\, Y_I + 2 X_{\Delta R} X_{\Delta I}\, Y_R\, Y_{\Delta I} \\ + 2 X_{\Delta R} X_{\Delta I}\, Y_{\Delta R}\, Y_I + 2 X_{\Delta R} X_{\Delta I}\, Y_{\Delta R}\, Y_{\Delta I} + X_I X_I\, Y_I\, Y_I + 2 X_I X_I\, Y_I\, Y_{\Delta I} + X_I X_I\, Y_{\Delta I}\, Y_{\Delta I} + 2 X_I X_{\Delta I}\, Y_I\, Y_I \\ + 4 X_I X_{\Delta I}\, Y_I\, Y_{\Delta I} + 2 X_I X_{\Delta I}\, Y_{\Delta I}\, Y_{\Delta I} + X_{\Delta I} X_{\Delta I}\, Y_I\, Y_I + 2 X_{\Delta I} X_{\Delta I}\, Y_I\, Y_{\Delta I} + X_{\Delta I} X_{\Delta I}\, Y_{\Delta I}\, Y_{\Delta I} \end{array} \right\rangle \end{aligned} \tag{A9}$$

When taking the expectation of each term in Equation A9, we can apply the identity for such an expectation of the product of Gaussian RVs: $\langle abcd \rangle = \langle ab \rangle \langle cd \rangle + \langle ac \rangle \langle bd \rangle + \langle ad \rangle \langle bc \rangle$ (Bendat & Piersol, 2010; Gardner & Yang, 1998). In the expanded result, which is not explicitly given here for brevity as it contains over 100 terms ($64 \times 3 = 192$ terms), we again apply the relations in Table A1. These steps yield the general solution for the first term of Equation A4b:

$$\left\langle \widetilde{Co}^{\,2}_{x_{total}\,y_{total}} \right\rangle = \frac{4}{L^2}\frac{L^2}{16}\begin{bmatrix} 2G_{xx}G_{yy} + 6Co^2_{xy} - 2Q^2_{xy} + 2G_{xx}G_{\Delta y\Delta y} + 2G_{yy}G_{\Delta x\Delta x} \\ + 12Co_{xy}Co_{\Delta x\Delta y} + 2G_{\Delta x\Delta x}G_{\Delta y\Delta y} + 6Co^2_{\Delta x\Delta y} \end{bmatrix}$$
$$= \frac{1}{2}\left[G_{xx}G_{yy} + 3Co^2_{xy} - Q^2_{xy} + G_{xx}G_{\Delta y\Delta y} + G_{yy}G_{\Delta x\Delta x} + 6Co_{xy}Co_{\Delta x\Delta y} + G_{\Delta x\Delta x}G_{\Delta y\Delta y} + 3Co^2_{\Delta x\Delta y}\right] \tag{A10}$$

Plugging in the general solutions from Equations A8 and A10 into Equation A4b, we obtain a general solution for the variance of Co-spectrum estimated from an instantaneous sample (i.e., A4b):

$$Var\left(\widetilde{Co}_{x_{total}\,y_{total}}\right) = \frac{1}{2}\begin{bmatrix} G_{xx}G_{yy} + Co^2_{xy} - Q^2_{xy} + G_{xx}G_{\Delta y\Delta y} + G_{yy}G_{\Delta x\Delta x} \\ + 2Co_{xy}Co_{\Delta x\Delta y} + G_{\Delta x\Delta x}G_{\Delta y\Delta y} + Co^2_{\Delta x\Delta y} \end{bmatrix} \tag{A11}$$

The corresponding uncertainty (i.e., Equation A4a) is given by taking the square root of Equation A11:

$$\Delta\left(\widetilde{Co}_{x_{total}\,y_{total}}\right) = \sqrt{\frac{1}{2}\begin{bmatrix} G_{xx}G_{yy} + Co^2_{xy} - Q^2_{xy} + G_{xx}G_{\Delta y\Delta y} + G_{yy}G_{\Delta x\Delta x} \\ + 2Co_{xy}Co_{\Delta x\Delta y} + G_{\Delta x\Delta x}G_{\Delta y\Delta y} + Co^2_{\Delta x\Delta y} \end{bmatrix}} \tag{A12}$$

Such uncertainty of Co-spectrum "rawly" estimated from an instantaneous sample is usually unacceptably large and must be reduced by averaging over many statistically independent samples. The variance of the mean spectrum of n statistically independent samples should scale with $\frac{1}{n}$ (Bendat & Piersol, 2010—see Chapter 9 "Statistical Errors in Advanced Estimates"). Note that the variance of a first-order sample mean scales with $\frac{1}{n}$, but the variance of a mean sample variance scales with $\frac{2}{n}$ (Gardner & Chu, 2020; Bendat & Piersol, 2010—see Chapter 8 "Statistical Errors in Basic Estimates"). On the aspect of uncertainty analysis, the variance of a mean sample spectrum should be quite different from the variance of a simple sample mean, but more comparable to the sample variance as both spectrum and variance are second-order statistics. However, it is necessary to consider that the DFT is a complex number, consisting of the real and imaginary parts. Because the real and imaginary parts are uncorrelated random variables with zero means and equal variances (Bendat & Piersol, 2010), each DFT calculation adds two statistical degrees of freedom to the estimate; therefore, the variance of the mean sample spectrum scales with $\frac{2}{2n} = \frac{1}{n}$. This situation may be understood through an analogy: An amplitude A is split into $a + ib$, where $\overline{a} = \overline{b} = \frac{A}{2}$; consequently, the square of amplitude becomes $\overline{a}^2 + \overline{b}^2 = \frac{A^2}{4} + \frac{A^2}{4} = \frac{A^2}{2}$, that is, half of the original amplitude square. Two variables n_d and n_p are used to denote the numbers of statistically independent samples for the statistical error and photon-noise-induced error, respectively, when averaging over the same many individual samples, due to the different correlation times of these two processes. We incorporate n_d into Equation A13 on the signal-driven terms (such as G_{xx}, G_{yy}, Co^2_{xy}, and Q^2_{xy}), and n_p on photon-noise-driven terms (such as $G_{\Delta x\Delta x}$, $G_{\Delta y\Delta y}$, and $Co_{\Delta x\Delta y}$). Both n_d and n_p are elaborated upon in the subsection of correlation times. We then reach the general equation for the uncertainty of a sample-averaged Co-spectrum

$$\left(\Delta\overline{Co_{x_{total}\,y_{total}}}\right)_{general} \simeq \sqrt{\begin{matrix} \frac{1}{2n_d}\left(G_{xx}G_{yy} + Co^2_{xy} - Q^2_{xy}\right) \\ + \frac{1}{2n_p}\left(G_{xx}G_{\Delta y\Delta y} + G_{yy}G_{\Delta x\Delta x} + 2Co_{xy}Co_{\Delta x\Delta y}\right) \\ + \frac{1}{2n_p}\left(G_{\Delta x\Delta x}G_{\Delta y\Delta y} + Co^2_{\Delta x\Delta y}\right) \end{matrix}} \tag{A13}$$

A2. Deriving Specific Uncertainties From the General Solutions

To derive a solution specific for an interleaved Co-spectrum, we recognize that the subsample noise does not correlate, making $Co_{\Delta x\Delta y} = 0$, so obtain the Co-spectral uncertainty for interleaved data:

$$(\Delta\overline{Co_{x_{total}\,y_{total}}}) \approx \sqrt{\frac{1}{2n_d}(G_{xx}G_{yy} + Co_{xy}^2 - Q_{xy}^2) + \frac{1}{2n_p}(G_{xx}G_{\Delta y\Delta y} + G_{yy}G_{\Delta x\Delta x} + G_{\Delta x\Delta x}G_{\Delta y\Delta y})} \tag{A14}$$

For the auto-spectrum, we adopt the special case that $X = Y$ resulting in $Q_{xx} = 0$, $Co_{xx} = G_{xx}$, and $Co_{\Delta x\Delta x} = G_{\Delta x\Delta x}$, giving the specific solution for the uncertainty of an auto-spectrum:

$$\Delta\overline{G_{x_{total}x_{total}}} = \sqrt{\frac{1}{n_d}G_{xx}^2 + \frac{1}{n_p}(2G_{xx}G_{\Delta x\Delta x} + G_{\Delta x\Delta x}^2)} \tag{A15}$$

A3. Applying These Equations to Interleaved Spectra

We now relate this derivation back to the interleaved method of the main text. Note that the uncertainty $\Delta\rho_{int}$ (which represents $\Delta\rho_A$ or $\Delta\rho_B$) of interleaved ρ'_A and ρ'_B is larger than the uncertainty $\Delta\rho$ of non-interleaved ρ', statistically $\langle|\Delta\rho_{int}|\rangle = \sqrt{2}\langle|\Delta\rho|\rangle$, due to the splitting of photon counts. To apply Equation A14 using parameters derived from interleaved and non-interleaved products, we make a few approximations indicated in Equation A16, where → indicates which main-text variables can be used in place of these appendix variables:

$$G_{xx} = G_{yy} \approx Co_{x_{total}\,y_{total}} \rightarrow Co\text{-}PSD_{\rho'_{A,Total}\rho'_{B,Total}} = Re(CPSD_{\rho'_{A,Total}\rho'_{B,Total}}) \tag{A16a}$$

$$Q_{x_{total}\,y_{total}} = Im(G_{x_{total}\,y_{total}}) \rightarrow Q\text{-}PSD_{\rho'_{A,Total}\rho'_{B,Total}} = Im(CPSD_{\rho'_{A,Total}\rho'_{B,Total}}) \tag{A16b}$$

$$G_{\Delta x\Delta x} = G_{\Delta y\Delta y} \approx 2(G_{x_{total}x_{total}} - Co_{x_{total}\,y_{total}}) \rightarrow PSD_{\Delta\rho_{int}} = 2(PSD_{\rho'_{Total}} - Co\text{-}PSD_{\rho'_{A,Total}\rho'_{B,Total}}) \tag{A16c}$$

where the factor of two in Equation A16c reflects the doubled noise variance due to the splitting of photon counts inherent to the interleaved method. Equation A15 can be expressed similarly using the following terms in Equation A17:

$$G_{xx} \approx Co_{x_{total}\,y_{total}} \rightarrow Co\text{-}PSD_{\rho'_{A,Total}\rho'_{B,Total}} \tag{A17a}$$

$$G_{\Delta x\Delta x} \approx (G_{x_{total}x_{total}} - Co_{x_{total}\,y_{total}}) \rightarrow PSD_{\Delta\rho} = (PSD_{\rho'_{Total}} - Co\text{-}PSD_{\rho'_{A,Total}\rho'_{B,Total}}) \tag{A17b}$$

where Equation A17b does not possess the factor of two of Equation A16c as the auto-spectrum is calculated using all available photons. Despite the two $G_{\Delta x\Delta x}$ in Equation A16c and A17b appearing identical, they represent two different noise levels (due to the photon count splitting) shown by their RHS differing by a factor of two.

Equations A16 and A17 enable:

$$\Delta\overline{Co\text{-}PSD} = \sqrt{\frac{1}{n_d}Co\text{-}PSD^2_{\rho'_{A,Total}\rho'_{B,Total}} - \frac{1}{2n_d}Q\text{-}PSD^2_{\rho'_{A,Total}\rho'_{B,Total}} + \frac{1}{n_p}Co\text{-}PSD_{\rho'_{A,Total}\rho'_{B,Total}}PSD_{\Delta\rho_{int}} + \frac{1}{2n_p}PSD^2_{\Delta\rho_{int}}} \tag{A18a}$$

$$\Delta\overline{PSD} = \sqrt{\frac{1}{n_d}Co\text{-}PSD^2_{\rho'_{A,Total}\rho'_{B,Total}} + \frac{2}{n_p}Co\text{-}PSD_{\rho'_{A,Total}\rho'_{B,Total}}PSD_{\Delta\rho} + \frac{1}{n_p}PSD^2_{\Delta\rho}} \tag{A18b}$$

Here, $PSD_{\Delta\rho_{int}} = 2PSD_{\Delta\rho}$

A4. Estimation of Correlation Times

The final step of deriving Equations A18a and 18b is to define the numbers of independent samples n_d and n_p by calculating the correlation times of the respective spectra. If successive samples of an atmospheric signal

correlate, then they cannot be considered as independent samples for statistical purposes. We define τ_C as the correlation time (also sometimes called the decorrelation time) of the atmospheric waves, which is the length of time over which the signal self-correlates to a significant degree. Similarly, the noise has a correlation time equal to the resolution Δt, as each instantaneous sample of the noise will be independent from each other. Thus, the true number of independent samples is $n_d = \frac{\tau_{obs}}{\tau_C}$ for signal-driven terms, and $n_p = \frac{\tau_{obs}}{\Delta t}$ for photon-noise-driven terms, where τ_{obs} is the total observation time included in the sample average. For example, 2,000 hr of observations of a process with a correlation time of 2 hr would yield 1,000 independent samples. For the noise spectra, where the signal can be approximated as white noise, the correlation time equals the sampling time, Δt. This fact ultimately means that the uncertainty is generally dominated by the statistical error but not the photon-noise-induced error.

The correlation time τ_C can be found using the autocorrelation function (acf) of the time series (Bendat & Piersol, 2010; Conan et al., 2000; O'Neill et al., 2004) or the spectra of the time series (Gardner & Chu, 2020; Gardner & Yang, 1998). A relatively simple approach using the acf is to calculate the time corresponding to the shift at which the acf has its first zero-crossing, which can be interpreted as a measure of the time over which the function self-correlates (Hinze, 1975). We employ this acf approach to estimate τ_C using a time series of density perturbations and average numerous estimates together to approximate a reasonable correlation time. The acf is calculated using a standard definition:

$$acf(k) = \frac{\frac{1}{N}\sum_{n=1}^{N-k}\left[x(t_n) - \bar{x}\right]\left[x(t_n + k) - \bar{x}\right]}{\overline{(x - \bar{x})^2}} \tag{A19}$$

where x is the density perturbation series, $\bar{x}$ is the mean of x, N is the length of the series, and k is the time lag. The correlation time found using this method is ∼1.4 hr in the winter when inspecting data with a time resolution of 1 hr and 0.48 km and ∼1.25 hr at a resolution of 0.5 hr and 0.96 km and are relatively stable with altitude from 30 to 50 km. Alternative methods to find this correlation time using the spectra themselves are provided by Gardner and Yang (1998) (see their Equations A15 and A16) and Gardner and Chu (2020) (see their Equation A5), and yield correlation times which are generally similar to but slightly longer than the acf results: ∼2.2 and ∼1.6 hr of each of the aforementioned resolutions, respectively. In general, we would comfortably state that the correlation time is on the higher end of 1–2 hr, so we select 1.7 hr for our calculations.

Overall, given the independent sample numbers n_d and n_p calculated using the different correlation times of the wave and noise derived above, we arrive at the final equations of spectral uncertainties used in the main text:

$$\Delta\overline{Co\text{-}PSD} = \sqrt{\frac{\tau_C}{\tau_{obs}}Co\text{-}PSD^2_{\rho'_{A,Total}\rho'_{B,Total}} - \frac{\tau_C}{2\tau_{obs}}Q\text{-}PSD^2_{\rho'_{A,Total}\rho'_{B,Total}} + \frac{\Delta t}{\tau_{obs}}Co\text{-}PSD_{\rho'_{A,Total}\rho'_{B,Total}}PSD_{\Delta\rho_{int}} + \frac{\Delta t}{2\tau_{obs}}PSD^2_{\Delta\rho_{int}}} \tag{A20a}$$

$$\Delta\overline{PSD} = \sqrt{\frac{\tau_C}{\tau_{obs}}Co\text{-}PSD^2_{\rho'_{A,Total}\rho'_{B,Total}} + \frac{2\Delta t}{\tau_{obs}}Co\text{-}PSD_{\rho'_{A,Total}\rho'_{B,Total}}PSD_{\Delta\rho} + \frac{\Delta t}{\tau_{obs}}PSD^2_{\Delta\rho}} \tag{A20b}$$

These equations are derived for the vertical wavenumber m-spectrum uncertainty. In principle, the ω-spectrum uncertainty can be derived similarly as demonstrated in Bendat and Piersol (2010). However, the relations among the time-series window length, correlation time, and the number of statistically independent samples must be carefully considered.

Appendix B: Comparison of Noise Floor Removal Methods

While Section 3.2 demonstrates the application of spectral interleaving methods to the derivation of a spectrum free of noise floor, it is valuable to compare the performance with the other noise-floor-removal methods presented in Section 2.1.

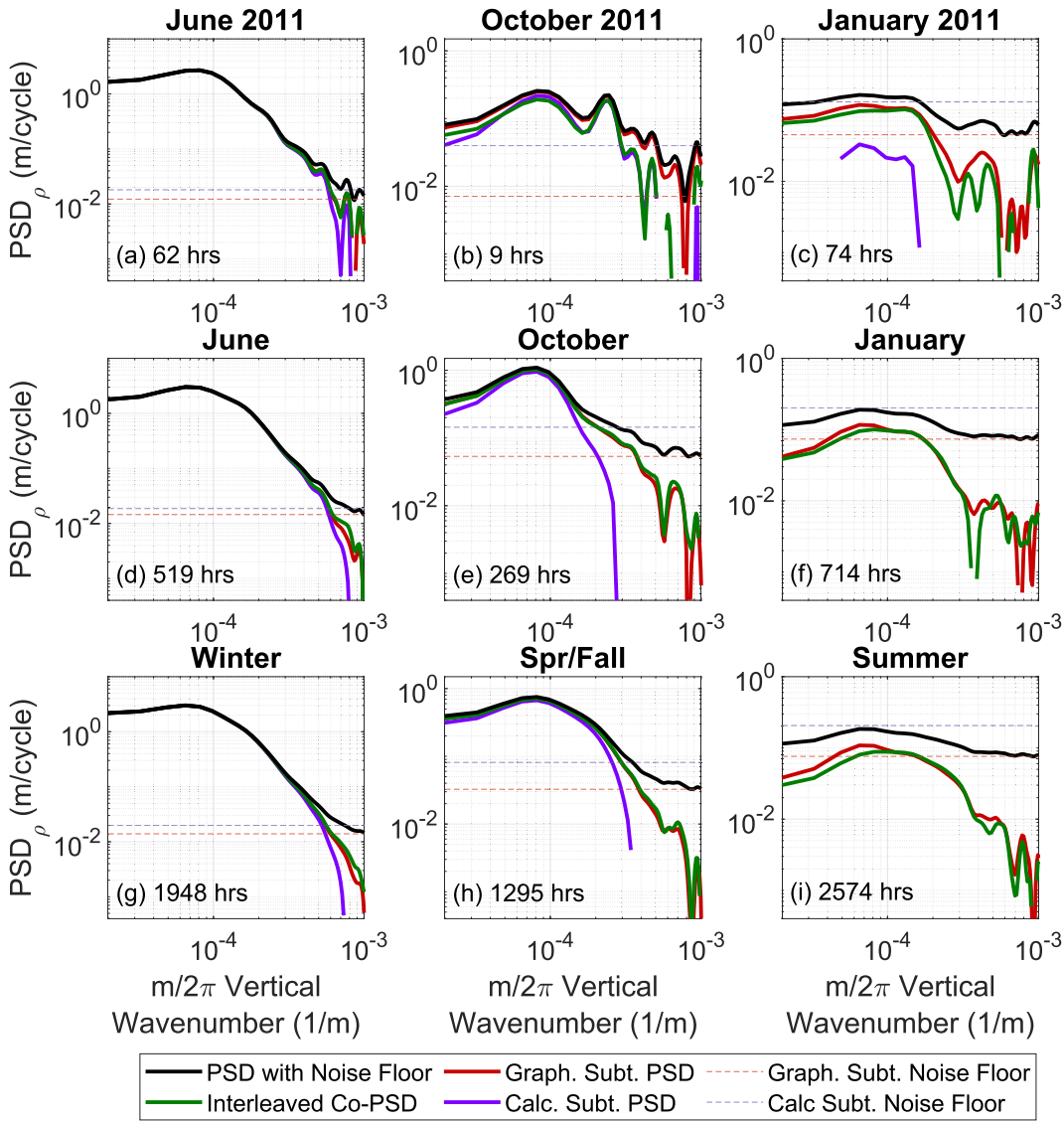

Figure B1. Same plot as Figure 4, but with the inclusion of the other noise-floor calculation methods as described in Section 2.1.

Assessing the calculative subtraction method (solid purple line) of Figure B1, we see that the method is able to identify a noise floor (dashed purple line) reasonably well in the winter, though spring/fall and summer show an overestimation of noise floor compared to how it would be visually identified. This results in the PSD corrected via this method yielding lower values than the other two methods in the m-regions affected by the noise floor. The summer results from this method show large overestimation, where Figures B1f and B1i even estimate a noise floor larger than the PSD entirely. This is likely a symptom of nonlinearities in the uncertainty definition used to calculate the floor, and while higher-order uncertainty estimates may improve its performance, the possibility of this behavior highlights the drawbacks of this method under a low-SNR. The graphical subtraction method (solid red line) yields results that largely agree with those of the interleaved method in most seasons in this test, though as previously mentioned, this depends on the method by which the noise floor is graphically determined.

Data Availability Statement

The data shown in this work can be downloaded in MatLab data format from Mendeley Data repository https://data.mendeley.com/datasets/b2r4dt3kf2/4 (Jandreau & Chu, 2024).

Acknowledgments
We highly appreciate Dr. Zukui Song for invaluable discussions on cross-spectrum and transfer function as well as Fourier transform and spectral analysis. We are grateful to Dr. Chester S. Gardner for his critical review comments and inspiring discussions. We gratefully acknowledge many graduate students and research scientists who made significant contributions to the McMurdo lidar campaign, and in particular special thanks to Zhibin Yu (2011), Brendan Roberts (2012), Weichun Fong (2013), Cao Chen (2014), Jian Zhao (2015), Ian Barry (2016), Zhengyu Hua (2017), Dongming Chang (2018), Zimu Li and Ian Geraghty (2019), Xianxin Li and Cissi Lin (2020), and Jackson Jandreau and Jack Iribarren (2023) who braved through the harsh Antarctica winters for lidar data collection. We are grateful to Yingfei Chen, Adam Peattie, Richard Dean, Nikolas Sinkola, Adam Godfrey, Pete Rossi, Mark Murphy, Hue Tran, and Kate McKenzie for their engineering help and support. We sincerely appreciate the staff of the United States Antarctic Program (USAP), McMurdo Station, Antarctica New Zealand (AntNZ), and Scott Base for their superb support over the years. The McMurdo lidar campaign was supported by a series of NSF Grants OPP-2110428, OPP-1443726, OPP-1246405, and OPP-0839091. This work was partially supported by NSF Grants OPP-2110428 and AGS-2029162, and by NASA Grants LWS 80NSSC23K0848 and FINESST 80NSSC22K1854. J. Jandreau is grateful to the generous support of FINESST Fellowship, Cooperative Institute for Research in Environmental Sciences (CIRES) Graduate Student Research Award, George C. and Joan A. Reid Memorial Scholarship, and Aerospace Engineering Sciences Smead Scholars Program.

References

Bendat, J. S., & Piersol, A. G. (2010). *Random data* (4th ed.). John Wiley.

Bevington, P. R., & Robinson, D. K. (2003). *Data reduction and error analysis for the physical sciences* (3rd ed.). McGraw-High Higher Education.

Blackman, R. B., & Tukey, J. W. (1958). The measurement of power spectra from the point of view of communications engineering—Part I. *The Bell System Technical Journal*, *37*(1), 185–282. https://doi.org/10.1002/j.1538-7305.1958.tb03874.x

Chen, C., Chu, X., Zhao, J., Roberts, B. R., Yu, Z., Fong, W., et al. (2016). Lidar observations of persistent gravity waves with periods of 3–10 h in the Antarctic middle and upper atmosphere at McMurdo (77.83°S, 166.67°E). *Journal of Geophysical Research: Space Physics*, *121*(2), 1483–1502. https://doi.org/10.1002/2015JA022127

Chu, X., Gardner, C. S., Li, X., & Lin, C. Y. (2022). Vertical transport of sensible heat and meteoric Na by the complete temporal spectrum of gravity waves in the MLT above McMurdo (77.84°S, 166.67°E), Antarctica. *Journal of Geophysical Research: Atmospheres*, *127*(16). https://doi.org/10.1029/2021JD035728

Chu, X., Huang, W., Fong, W., Yu, Z., Wang, Z., Smith, J. A., & Gardner, C. S. (2011). First Lidar observations of polar mesospheric clouds and Fe temperatures at McMurdo (77.8°S, 166.7°E), Antarctica. *Geophysical Research Letters*, *38*(16), L16810. https://doi.org/10.1029/2011GL048373

Chu, X., Nishimura, Y., Xu, Z., Yu, Z., Plane, J. M. C., Gardner, C. S., & Ogawa, Y. (2020). First simultaneous Lidar observations of thermosphere-ionosphere Fe and Na (TIFe and TINa) layers at McMurdo (77.84°S, 166.67°E), Antarctica with concurrent measurements of aurora activity, enhanced ionization layers, and converging electric field. *Geophysical Research Letters*, *47*(20), e2020GL090181. https://doi.org/10.1029/2020GL090181

Chu, X., Pan, W., Papen, G. C., Gardner, C. S., & Gelbwachs, J. A. (2002). Fe Boltzmann temperature Lidar: Design, error analysis, and initial results at the North and South Poles. *Applied Optics*, *41*(21), 4400. https://doi.org/10.1364/AO.41.004400

Chu, X., & Papen, G. C. (2005). Resonance fluorescence Lidar for measurements of the middle and upper atmosphere. In T. Fujii & T. Fukuchi (Eds.), *Laser remote sensing* (pp. 179–432). CRC Press, Taylor and Francis Group.

Chu, X., Yu, Z., Gardner, C. S., Chen, C., & Fong, W. (2011). Lidar observations of neutral Fe layers and fast gravity waves in the thermosphere (110-155 km) at McMurdo (77.8°S, 166.7°E), Antarctica. *Geophysical Research Letters*, *38*(23), L23807. https://doi.org/10.1029/2011GL050016

Chu, X., Zhao, J., Lu, X., Harvey, V. L., Jones, R. M., Becker, E., et al. (2018). Lidar observations of stratospheric gravity waves from 2011 to 2015 at McMurdo (77.84°S, 166.69°E), Antarctica: 2. Potential energy densities, lognormal distributions, and seasonal variations. *Journal of Geophysical Research: Atmospheres*, *123*(15), 7910–7934. https://doi.org/10.1029/2017JD027386

Conan, R., Borgnino, J., Ziad, A., & Martin, F. (2000). Analytical solution for the covariance and for the decorrelation time of the angle of arrival of a wave front corrugated by atmospheric turbulence. *Journal of the Optical Society of America A*, *17*(10), 1807. https://doi.org/10.1364/JOSAA.17.001807

Desaubies, Y. J. F. (1976). Analytical representation of internal wave spectra. *Journal of Physical Oceanography*, *6*, 976–981. https://doi.org/10.1175/1520-0485(1976)006<0976:AROIWS>2.0.CO;2

Dewan, E. M., & Grossbard, N. (2000). Power spectral artifacts in published balloon data and implications regarding saturated gravity wave theories. *Journal of Geophysical Research*, *105*(D4), 4667–4683. https://doi.org/10.1029/1999JD901108

Gardner, C. S., & Chu, X. (2020). Eliminating photon noise biases in the computation of second-order statistics of Lidar temperature, wind, and species measurements. *Applied Optics*, *59*(27), 8259–8271. https://doi.org/10.1364/AO.400375

Gardner, C. S., & Liu, A. Z. (2014). Measuring eddy heat, constituent, and momentum fluxes with high-resolution Na and Fe Doppler Lidars. *Journal of Geophysical Research: Atmospheres*, *119*(17), 10583–10603. https://doi.org/10.1002/2013JD021074

Gardner, C. S., Senft, D. C., Beatty, T. J., Bills, R. E., & Hostetler, C. A. (1989). Rayleigh and sodium Lidar techniques for measuring middle atmospheric density, temperature and wind perturbations and their spectra. In C. H. Liu & B. Edwards (Eds.), *World ionosphere/thermosphere study handbook* (Vol. 2, pp. 148–187). Ill: Int. Congr. of Sci. Unions.

Gardner, C. S., & Yang, W. (1998). Measurements of the dynamical cooling rate associated with the vertical transport of heat by dissipating gravity waves in the mesopause region at the Starfire Optical Range, New Mexico. *Journal of Geophysical Research*, *103*(D14), 16909–16926. https://doi.org/10.1029/98JD00683

Gelbwachs, J. A. (1994). Iron Boltzmann factor LIDAR: Proposed new remote-sensing technique for mesospheric temperature. *Applied Optics*, *33*(30), 7151–7156. https://doi.org/10.1364/ao.33.007151

Heinzel, G., Rüdiger, A., & Schilling, R. (2002). Spectrum and spectral density estimation by the Discrete Fourier transform (DFT), including a comprehensive list of window functions and some new at-top windows. https://hdl.handle.net/11858/00-001M-0000-0013-557A-5

Hinze, J. O. (1975). *Turbulence* (2nd ed.). McGraw-Hill.

Jandreau, J., & Chu, X. (2022). Comparison of three methodologies for removal of random-noise-induced biases from second-order statistical parameters of Lidar and radar measurements. *Earth and Space Science*, *9*(1), e2021EA002073. https://doi.org/10.1029/2021EA002073

Jandreau, J., & Chu, X. (2024). Bias-eliminating techniques in the computation of power spectra for characterizing gravity waves (version 4) [Dataset]. *Mendeley Data*. https://data.mendeley.com/datasets/b2r4dt3kf2/4

Li, Z., Chu, X., Harvey, V. L., Jandreau, J., Lu, X., Yu, Z., et al. (2020). First Lidar observations of Quasi-Biennial oscillation-induced interannual variations of gravity wave potential energy density at McMurdo via a modulation of the Antarctic polar vortex. *Journal of Geophysical Research: Atmospheres*, *125*(16), e2020JD032866. https://doi.org/10.1029/2020JD032866

Lu, X., Chu, X., Fong, W., Chen, C., Yu, Z., Roberts, B. R., & McDonald, A. J. (2015). Vertical evolution of potential energy density and vertical wave number spectrum of Antarctic gravity waves from 35 to 105 km at McMurdo (77.8°S, 166.7°E): GW energy density and wavenumber spectra. *Journal of Geophysical Research: Atmospheres*, *120*(7), 2719–2737. https://doi.org/10.1002/2014JD022751

O'Neill, P. L., Nicolaides, D., Honnery, D., & Soria, J. (2004). Autocorrelation functions and the determination of integral length with reference to experimental and numerical data. In *15th Australasian Fluid Mechanics Conference*.

Owens, A. J. (1978). An algorithm for generating fluctuations having any arbitrary power spectrum. *Journal of Geophysical Research*, *83*(A4), 1673–1675. https://doi.org/10.1029/JA083iA04p01673

Senft, D. C., & Gardner, C. S. (1991). Seasonal variability of gravity wave activity and spectra in the mesopause region at Urbana. *Journal of Geophysical Research*, *96*(D9), 17229–17264. https://doi.org/10.1029/91JD01662

Smith, S. A., Fritts, D. C., & Vanzandt, T. E. (1987). Evidence for a saturated spectrum of atmospheric gravity waves. *Journal of the Atmospheric Sciences*, *44*(10), 1404–1410. https://doi.org/10.1175/1520-0469(1987)044<1404:EFASSO>2.0.CO;2

Stull, R. B. (1999). *An introduction to boundary layer meteorology, by R. B. Stull. Atmospheric sciences library*. Springer.

Taylor, J. R. (1997). *An introduction to error analysis – the study of uncertainties in physical measurements* (2nd ed.). University Science Books.

Tsuda, T., Inoue, T., Fritts, D. C., VanZandt, T. E., Kato, S., Sato, T., & Fukao, S. (1989). MST radar observations of a saturated gravity wave spectrum. *Journal of the Atmospheric Sciences*, *46*(15), 2440–2447. https://doi.org/10.1175/1520-0469(1989)046<2440:MROOAS>2.0.CO;2

VanZandt, T. E. (1982). A universal spectrum of buoyancy waves in the atmosphere. *Geophysical Research Letters*, *9*(5), 575–578. https://doi.org/10.1029/GL009i005p00575

von Storch, H., & Zwiers, F. W. (1999). *Statistical analysis in climate research* (1st ed.). Cambridge University Press.

Whiteway, J. A., & Carswell, A. I. (1995). Lidar observations of gravity wave activity in the upper stratosphere over Toronto. *Journal of Geophysical Research*, *100*(D7), 14113–14124. https://doi.org/10.1029/95JD00511

Wilson, R., Chanin, M. L., & Hauchecorne, A. (1991). Gravity waves in the middle atmosphere observed by Rayleigh Lidar: 2. Climatology. *Journal of Geophysical Research*, *96*(D3), 5169–5183. https://doi.org/10.1029/90JD02610

Zhao, J., Chu, X., Chen, C., Lu, X., Fong, W., Yu, Z., et al. (2017). Lidar observations of stratospheric gravity waves from 2011 to 2015 at McMurdo (77.84°S, 166.69°E), Antarctica: 1. Vertical wavelengths, periods, and frequency and vertical wave number spectra. *Journal of Geophysical Research: Atmospheres*, *122*(10), 5041–5062. https://doi.org/10.1002/2016JD026368